Space Sci Rev (2007) 131: 3–39
DOI 10.1007/s11214-007-9247-6

MESSENGER Mission Overview

Sean C. Solomon · Ralph L. McNutt, Jr. · Robert E. Gold · Deborah L. Domingue

Received: 9 January 2007 / Accepted: 13 July 2007 / Published online: 5 October 2007

Abstract The MErcury Surface, Space ENvironment, GEochemistry, and Ranging (MESSENGER) spacecraft, launched on August 3, 2004, is nearing the halfway point on its voyage to become the first probe to orbit the planet Mercury. The mission, spacecraft, and payload are designed to answer six fundamental questions regarding the innermost planet: (1) What planetary formational processes led to Mercury's high ratio of metal to silicate? (2) What is the geological history of Mercury? (3) What are the nature and origin of Mercury's magnetic field? (4) What are the structure and state of Mercury's core? (5) What are the radar-reflective materials at Mercury's poles? (6) What are the important volatile species and their sources and sinks near Mercury? The mission has focused to date on commissioning the spacecraft and science payload as well as planning for flyby and orbital operations. The second Venus flyby (June 2007) will complete final rehearsals for the Mercury flyby operations in January and October 2008 and September 2009. Those flybys will provide opportunities to image the hemisphere of the planet not seen by Mariner 10, obtain high-resolution spectral observations with which to map surface mineralogy and assay the exosphere, and carry out an exploration of the magnetic field and energetic particle distribution in the near-Mercury environment. The orbital phase, beginning on March 18, 2011, is a one-year-long, near-polar-orbital observational campaign that will address all mission goals. The orbital phase will complete global imaging, yield detailed surface compositional and topographic data over the northern hemisphere, determine the geometry of Mercury's internal magnetic field and magnetosphere, ascertain the radius and physical state of Mercury's outer core, assess the nature of Mercury's polar deposits, and inventory exospheric neutrals and magnetospheric charged particle species over a range of dynamic conditions. Answering the questions that have guided the MESSENGER mission will expand our understanding of the formation and evolution of the terrestrial planets as a family.

S.C. Solomon (✉)
Department of Terrestrial Magnetism, Carnegie Institution of Washington, Washington, DC 20015, USA
e-mail: scs@dtm.ciw.edu

R.L. McNutt, Jr. · R.E. Gold · D.L. Domingue
The Johns Hopkins University Applied Physics Laboratory, Laurel, MD 20723, USA

Keywords Mercury · MESSENGER · Planet formation · Geological history · Magnetosphere · Exosphere

1 Introduction

Mercury is the least studied of the inner planets. A substantially improved knowledge of the planet Mercury is nonetheless critical to our understanding of how the terrestrial planets formed and evolved. Determining the surface composition of Mercury, a body with a ratio of metal to silicate higher than any other planet or satellite, will provide a unique window on the processes by which planetesimals in the primitive solar nebula accreted to form planets. Documenting the global geological history will elucidate the roles of planet size and solar distance as governors of magmatic and tectonic history for a terrestrial planet. Characterizing the nature of the magnetic field of Mercury and the size and state of Mercury's core will allow us to generalize our understanding of the energetics and lifetimes of magnetic dynamos, as well as core and mantle thermal histories, in solid planets and satellites. Determining the nature of the volatile species in Mercury's polar deposits, atmosphere, and magnetosphere will provide critical insight into volatile inventories, sources, and sinks in the inner solar system.

MESSENGER is a MErcury Surface, Space ENvironment, GEochemistry, and Ranging mission designed to achieve these aims. As part of the Discovery Program of the U.S. National Aeronautics and Space Administration (NASA), the MESSENGER spacecraft will orbit Mercury for one Earth year after completing three flybys of that planet following two flybys of Venus and one of Earth. The Mercury flybys will return significant new data early in the mission, while the orbital phase, guided by the flyby data, will enable a focused scientific investigation of the innermost planet. Answers to key questions about Mercury's high density, crustal composition and structure, volcanic history, core structure, magnetic field generation, polar deposits, atmosphere, overall volatile inventory, and magnetosphere will be provided by an optimized set of seven miniaturized scientific instruments. In this paper we first describe the rationale for and scientific objectives of the MESSENGER mission. We then summarize the mission implementation plan designed to satisfy those objectives. Companion papers in this issue provide detailed descriptions of the MESSENGER spacecraft (Leary et al. 2007) and mission design (McAdams et al. 2007), mission (Holdridge and Calloway 2007) and science operations centers (Winters et al. 2007), payload instruments (Anderson et al. 2007; Andrews et al. 2007; Cavanaugh et al. 2007; Goldsten et al. 2007; Hawkins et al. 2007; McClintock and Lankton 2007; Schlemm et al. 2007), and radio science (Srinivasan et al. 2007), as well as more expansive summaries of the principal scientific issues to be addressed by a Mercury orbiter mission (Boynton et al. 2007; Domingue et al. 2007; Head et al. 2007; Slavin et al. 2007; Zuber et al. 2007).

2 Context for MESSENGER Selection

The selection of MESSENGER as a NASA Discovery Program mission was a decision rooted in a 25-year history of Mercury exploration and strategic planning for improving our understanding of the inner planets.

The only spacecraft to visit Mercury to date was Mariner 10. In the course of three flybys of the planet in 1974 and 1975, Mariner 10 imaged about 45% of Mercury's surface

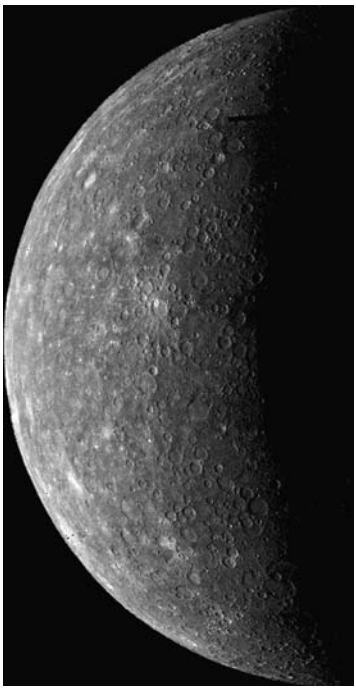

Fig. 1 Mosaic of images of Mercury obtained by the Mariner 10 spacecraft on the incoming portion of its first flyby of Mercury (Robinson et al. 1999)

(Fig. 1) at an average resolution of about 1 km and less than 1% of the surface at better than 500-m resolution (Murray 1975). Mariner 10 discovered the planet's internal magnetic field (Ness et al. 1974, 1975); measured the ultraviolet signatures of H, He, and O in Mercury's tenuous atmosphere (Broadfoot et al. 1974, 1976); documented the time-variable nature of Mercury's magnetosphere (Ogilvie et al. 1974; Simpson et al. 1974); and determined some of the physical characteristics of Mercury's surface materials (Chase et al. 1974).

Immediately following the Mariner 10 mission, a Mercury orbiter was widely recognized as the obvious next step in the exploration of the planet (COMPLEX 1978). Further, the primary objectives of such an orbiter mission were defined: "to determine the chemical composition of the planet's surface on both a global and regional scale, to determine the structure and state of the planet's interior, and to extend the coverage and improve the resolution of orbital imaging" (COMPLEX 1978). In the late 1970s, however, it was thought that the change in spacecraft velocity required for orbit insertion around Mercury was too large for conventional propulsion systems, and this belief colored the priority placed on further exploration of the innermost planet (COMPLEX 1978).

In the mid-1980s, about a decade after the end of the Mariner 10 mission, multiple gravity-assist trajectories were discovered that could achieve Mercury orbit insertion with chemical propulsion systems (Yen 1985, 1989). This finding stimulated detailed studies of Mercury orbiter missions in Europe and the United States between the mid-1980s and early 1990s (Neukum et al. 1985; Belcher et al. 1991). During the same time interval there were important discoveries made by ground-based astronomy, including the Na and K components of Mercury's atmosphere (Potter and Morgan 1985, 1986) and the radar-reflective deposits at Mercury's north and south poles (Harmon and Slade 1992; Slade et al. 1992). A re-examination of the primary objectives of a Mercury orbiter mission during that period affirmed those defined earlier and added "that characterization of

Mercury's magnetic field be [an additional] primary objective for exploration of that planet" (COMPLEX 1990).

In the early 1990s, after re-examining its approach to planetary exploration, NASA initiated the Discovery Program, intended to foster more frequent launches of less costly, more focused missions selected on the basis of rigorous scientific and technical competition. Mercury was the target of a number of early unsuccessful proposals to the Discovery Program for flyby and orbiter missions (Nelson et al. 1994; Spudis et al. 1994; Clark et al. 1999). The MESSENGER concept was initially proposed to the NASA Discovery Program in 1996, and after multiple rounds of evaluation (McNutt et al. 2006) the mission was selected for flight in July 1999.

In parallel with the selection, development, and launch of MESSENGER, the European Space Agency (ESA) and the Institute of Space and Astronautical Science (ISAS) of the Japan Aerospace Exploration Agency (JAXA) have approved and are currently developing the BepiColombo mission to send two spacecraft into Mercury orbit (Grard et al. 2000; Anselmi and Scoon 2001). BepiColombo was selected by ESA as its fifth cornerstone mission in 2000, and ISAS announced its intent to collaborate on the project that same year. The two spacecraft, scheduled for launch on a single rocket in 2013, will be in coplanar polar orbits. An ESA-supplied Mercury Planetary Orbiter will emphasize observations of the planet, and an ISAS-supplied Mercury Magnetospheric Orbiter will emphasize observations of the magnetosphere and its interactions with the solar wind. Payload instruments on the two spacecraft were selected in 2004 (Hayakawa et al. 2004; Schulz and Benkhoff 2006).

3 Guiding Science Questions

The MESSENGER mission was designed to address six key scientific questions, the answers to which bear not only on the nature of the planet Mercury but also more generally on the origin and comparative evolution of the terrestrial planets as a class.

3.1 What Planetary Formational Processes Led to the High Ratio of Metal to Silicate in Mercury?

Mercury's uncompressed density (about 5.3 Mg/m^3), the highest of any planet, has long been taken as evidence that iron is the most abundant contributor to the bulk composition. Interior structure models in which a core has fully differentiated from the overlying silicate mantle indicate that the core radius is approximately 75% of the planetary radius and the fractional core mass is about 60% if the core is pure iron (Siegfried and Solomon 1974); still larger values are possible if the core has a light element such as sulfur alloyed with the iron (Harder and Schubert 2001). Such a metallic mass fraction is at least twice that of the Earth (Fig. 2), Venus, or Mars.

Calculations of dynamically plausible scenarios for the accretion of the terrestrial planets permit a wide range of outcomes for Mercury. Given an initial protoplanetary nebular disk of gas and dust, planetesimals accrete to kilometer size in 10^4 years (Weidenschilling and Cuzzi 1993), and runaway growth of planetary embryos of Mercury- to Mars-size accrete by the gravitational accumulation of planetesimals in 10^5 years (Kortenkamp et al. 2000). During runaway growth, Mercury-size bodies can experience substantial migrations of their semimajor axes (Wetherill 1988). Further, each of the terrestrial planets probably formed from material originally occupying a wide range in solar distance, although some correlation

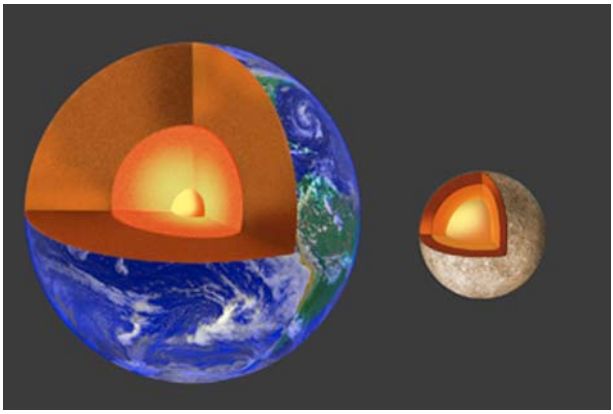

Fig. 2 Schematic cut-away views of the fractional volumes occupied by the central metallic cores of Mercury and Earth. The solid inner core and fluid outer core of the Earth are shown to approximate scale. Mercury's outer core is likely fluid (Margot et al. 2007), but the core radius and the nature of any inner core remain to be determined

is expected between the final heliocentric distance of a planet and those of the planetesimals from which it formed (Wetherill 1988, 1994).

Three explanations for the high metal fraction of Mercury have been put forward. The first invokes differences in the response of iron and silicate particles to aerodynamic drag by nebular gas to achieve fractionation at the onset of planetesimal accretion (Weidenschilling 1978). The second and third explanations invoke processes late in the planetary accretion process, after the Mercury protoplanet had differentiated silicate mantle from metal core. In one, the high metal content of Mercury is attributed to preferential vaporization of silicates by radiation from a hot nebula and removal by a strong solar wind (Cameron 1985; Fegley and Cameron 1987). In the other, selective removal of silicate occurred as a result of a giant impact (Benz et al. 1988; Wetherill 1988, 1994).

These three hypotheses lead to different predictions for the bulk chemistry of the silicate fraction of Mercury (Lewis 1988; Boynton et al. 2007). Under the giant impact hypothesis, the residual silicate material on Mercury would be dominantly of mantle composition. The FeO content would reflect the oxidation state of the material from which the protoplanet accreted, but the loss of much of the original crust would deplete Ca, Al, and alkali metals without enriching refractory elements. The vaporization model, in contrast, predicts strong enrichment of refractory elements and depletion of alkalis and FeO (Fegley and Cameron 1987). Under both of these hypotheses, the present crust should represent primarily the integrated volume of magma produced by partial melting of the relic mantle. Under the aerodynamic sorting proposal (Weidenschilling 1978), the core and silicate portions of Mercury can be prescribed by nebular condensation models, suitably weighted by solar distance, except that the ratio of metal to silicate is much larger (Lewis 1988). This hypothesis permits a thick primordial crust, i.e., one produced by crystal-liquid fractionation of a silicate magma ocean. Determining the bulk chemistry of the silicate portion of Mercury thus offers an opportunity to discern those processes operating during the formation of the inner solar system that had the greatest influence on producing the distinct compositions of the inner planets.

Present information on the chemistry and mineralogy of the surface of Mercury, however, is too limited to distinguish clearly among the competing hypotheses. Ground-based reflectance spectra at visible and near-infrared wavelengths do not show a consistent absorption feature near 1 μm diagnostic of Fe^{2+} (Vilas 1985; Warell et al. 2006), limiting the average FeO content to be less than about 3–4 weight percent (Blewett et al. 1997). Very reduced compositions comparable to enstatite achondrite meteorites with less than 0.1% FeO are compatible with Mercury's reflectance, although a generally red spectral slope is

thought to be the result of nanophase iron metal, altered by space weathering from silicates originally containing a few percent FeO (Burbine et al. 2002). Earth-based mid-infrared observations show emission features consistent with the presence of both calcic plagioclase feldspar containing some sodium and very-low-FeO pyroxene; variations in spectral features with Mercury longitude indicate that surface mineralogical composition is spatially heterogeneous (Sprague et al. 2002). Mature lunar highland anorthosite soils are regarded as good general spectral analogues to Mercury surface materials (Blewett et al. 2002).

On the basis of the low FeO content of Mercury's surface materials inferred from Earth-based spectra and Mariner 10 color images, surface units interpreted as volcanic in origin are thought to average no more than about 3% FeO by weight (Robinson and Taylor 2001). On the grounds that the solid/liquid partition coefficient for FeO during partial melting of mantle material is near unity, the mantle FeO abundance has been inferred to be comparable (Robinson and Taylor 2001). This deduction, together with a general increase in bulk silicate FeO content with solar distance for the terrestrial planets and the eucrite parent body, has been taken to suggest both that the inner solar nebula displayed a radial gradient in FeO and that Mercury was assembled dominantly from planetesimals that formed at solar distances similar to that of Mercury at present (Robinson and Taylor 2001).

Substantial progress on understanding the composition of Mercury must await remote sensing by an orbiting spacecraft (Boynton et al. 2007). Also important to an assessment of bulk composition and formation hypotheses would be an estimate of the thickness of Mercury's crust. Variations in crustal thickness can be estimated by a combined analysis of gravity and topography measurements (Zuber et al. 2007). Moreover, an upper bound on mean crustal thickness can be obtained from isostatically compensated long-wavelength topographic variations, on the grounds that the temperature at the base of the crust cannot have been so high that variations in crustal thickness were removed by viscous flow on timescales shorter than the age of the crust (Nimmo 2002).

3.2 What Is the Geological History of Mercury?

A generalized geological history of Mercury has been developed from Mariner 10 images (Head et al. 2007). The 45% of Mercury's surface imaged by Mariner 10 can be divided into four major terrains (Spudis and Guest 1988). Heavily cratered regions have an impact crater density suggesting that this terrain records the period of heavy bombardment that ended about 3.8 Ga on the Moon (Neukum et al. 2001). Intercrater plains, the most extensive terrain type, were emplaced over a range of ages during the period of heavy bombardment. Hilly and lineated terrain occurs antipodal to the Caloris basin—at 1,300 km in diameter the largest and youngest (Neukum et al. 2001) well-preserved impact structure on Mercury—and is thought to have originated at the time of the Caloris impact by the focusing of impact-generated shock and seismic waves. Smooth plains, cover 40% of the area imaged by Mariner 10. Smooth plains are the youngest terrain type and are mostly associated with large impact basins. They are in a stratigraphic position similar to that of the lunar maria. On the basis of the areal density of impact craters on the portion of Mercury's surface imaged by Mariner 10, as well as the scaling of cratering flux from the Moon to Mercury, smooth plains emplacement may have ended earlier on Mercury than did mare volcanism on the Moon (Neukum et al. 2001).

The role of volcanism in Mercury's geological history, however, is uncertain. Both volcanic and impact ejecta emplacement mechanisms have been suggested for the intercrater and smooth plains, and the issue remains unresolved because no diagnostic morphological features capable of distinguishing between the two possibilities are clearly visible at the

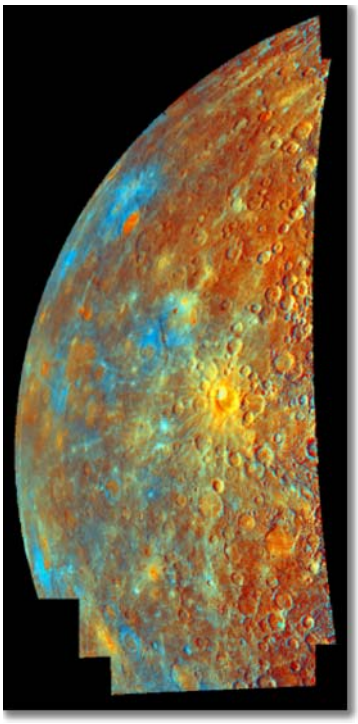

Fig. 3 Enhanced color composite showing portions of the incoming hemisphere of Mercury during the first Mariner 10 encounter (Robinson and Lucey 1997). The red component is the inverse of the opaque index (increasing redness indicates decreasing opaque mineralogy), the green component is the iron-maturity parameter, and blue shows the relative visible color. Smooth plains units (*center left*) display distinct colors and embaying boundaries consistent with material emplaced as a fluid flow. Both characteristics support the hypothesis that the plains are volcanic in origin. Other color variations have been interpreted as evidence for pyroclastic material, differences in composition between impact-excavated material and its surroundings, and differences in soil maturity (Robinson and Lucey 1997)

typical resolution of Mariner 10 images (Milkovich et al. 2002). Ground-based infrared and millimeter observations of Mercury have been interpreted as indicating a generally basalt-free surface and thus a magmatic history dominated either by intrusions or by eruptions of only low-FeO (FeO plus TiO_2 less than 6% by weight) lavas (Jeanloz et al. 1995). Recalibration of Mariner 10 color images and reprojection using color parameters sensitive to iron content, soil maturity, and opaque mineral abundances (Robinson and Lucey 1997) indicate that geological units are distinguishable on the basis of color (Fig. 3). In particular, the correlation of color boundaries with lobate boundaries of smooth plains previously mapped from Mariner 10 images supports the inference that the plains units are volcanic deposits compositionally distinct from underlying older crustal material (Robinson and Lucey 1997).

Mercury's tectonic history is unlike that of any other terrestrial planet. The most prominent tectonic features on the surface are lobate scarps, 20 to 500 km in length and hundreds of meters to several kilometers in height (Watters et al. 1998). On the basis of their asymmetric cross sections, rounded crests, sinuous but generally linear to arcuate planforms, and transection relationships with craters, the scarps (Fig. 4) are interpreted to be the surface expression of major thrust faults (Strom et al. 1975). Because the scarps are more or less evenly distributed over the well-imaged portion of the surface and display a broad range of azimuthal trends, they are thought to be the result of global contraction of the planet. From the lengths and heights of the scarps, and from simple geometric fault models or fault length-displacement relationships, the inferred 0.05–0.10% average contractional strain if extrapolated to the full surface area of the planet would be equivalent to a decrease of 1–2 km in planetary radius (Strom et al. 1975; Watters et al. 1998). Scarp development postdated the intercrater plains, on the grounds

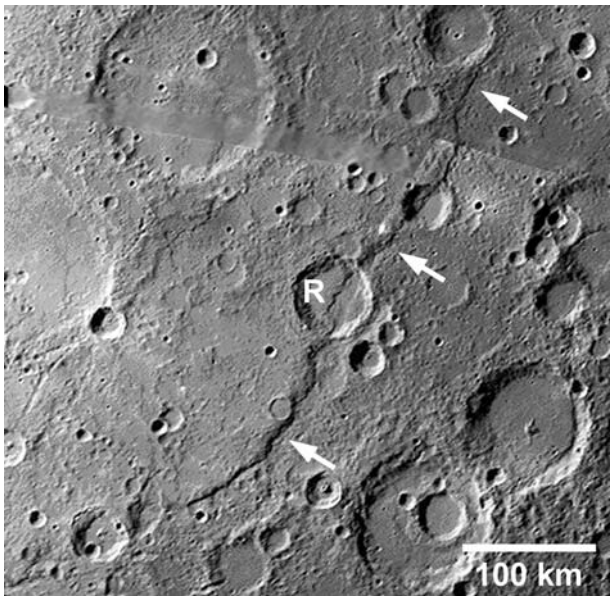

Fig. 4 Mariner 10 image mosaic of Discovery Rupes, the longest known lobate scarp on Mercury (Strom et al. 1975). The scarp is 550 km long and displays 1 km or more of topographic relief (Watters et al. 1998). *Arrows* denote the approximate direction of underthrusting of the crustal block on the right beneath the block to the left. The crater Rameau (*R*), transected by the scarp, is 60 km in diameter. Image courtesy M.S. Robinson

that no scarps are embayed by such plains material, and extended until after emplacement of smooth plains units (Strom et al. 1975).

This estimate of global contraction poses a potentially strong constraint on models for cooling of Mercury's interior. Thermal history calculations that incorporate parameterized core and mantle convection as well as the generation and upward transport of mantle partial melt (Hauck et al. 2004) indicate that models consistent with 0.05–0.10% surface contraction since the end of heavy bombardment are limited to those with a mantle rheology appropriate to anhydrous conditions, modest concentrations of heat-producing elements, and a significant fraction of a light alloying element (e.g., S) in the core to limit inner core solidification. A further constraint on thermal models may come from estimates of the depth of faulting that accompanied scarp formation. Modeling of topographic profiles across several of Mercury's longest known scarps yields inferred depths of faulting of 30–40 km, and from an estimate of the temperature limiting brittle behavior a thermal gradient may be derived (Watters et al. 2002; Nimmo and Watters 2004), although the age appropriate to that estimate and the degree to which it is representative of the global average gradient at that time are not known.

Recent ground-based imaging has yielded information on the hemisphere of Mercury not viewed by Mariner 10. Optical to near-infrared images of the sunlit portion of Mercury have been made by several groups using short-exposure, high-definition techniques (Baumgardner et al. 2000; Dantowitz et al. 2000; Warell and Limaye 2001; Ksanfomality et al. 2005; Warell and Valegård 2006; Ksanfomality and Sprague 2007). Resolution of the best such images approaches 200 km, and both bright and dark features appear in common locations on those portions of the surface imaged with independent methods (Mendillo et al. 2001). Dark features are thought to be plains (Mendillo et al. 2001), and a majority of the bright features are likely to be young rayed craters, which have comparable densities on Mercury's two hemispheres (Warell and Limaye 2001). A large basin comparable in diameter to Caloris has been identified at about 8°N, 80°E (Ksanfomality et al. 2005). Radar images at a resolution as good as 1.5–3 km have been obtained of a number of radar-bright fea-

tures on the side of Mercury not imaged by Mariner 10 (Harmon 1997, 2002; Harmon et al. 2007). At the highest resolution these features appear to be of impact origin (Harmon 2002; Harmon et al. 2007), including one previously speculated to be a volcanic construct on the basis of earlier radar images of coarser resolution (Harmon 1997).

To make a substantial improvement in our knowledge of the full geological history of Mercury, global multicolor imaging of the surface from an orbiting spacecraft is required. Average resolution should be significantly better than that typical of Mariner 10 images, and a capability for targeted high-resolution imaging is desirable. Topographic information would aid in landform identification and could be obtained from an altimeter, stereo photogrammetry (Cook and Robinson 2000), or a combination of the two methods.

3.3 What Are the Nature and Origin of Mercury's Magnetic Field?

Mercury's intrinsic magnetic field, discovered by Mariner 10 (Ness et al. 1976), has a dipole component nearly orthogonal to Mercury's orbital plane and a moment near 300 nT-R_M^3, where R_M is Mercury's mean radius (Connerney and Ness 1988). The origin of this field, however, is not understood (Stevenson 2003). Mercury's magnetic field cannot be externally induced on the grounds that the measured planetary field is far greater in magnitude than the interplanetary field (Connerney and Ness 1988). The dipole field could be a remanent or fossil field acquired during lithospheric cooling in the presence of an internal or external field (Srnka 1976; Stephenson 1976), or it could be the product of a modern core dynamo (Schubert et al. 1988; Stevenson 2003). Permanent magnetization from an external source has been discounted on the grounds that a thick shell of coherently magnetized material is needed to match the observed dipole moment, and the lithosphere of Mercury would not have been able to cool and thicken sufficiently in the time interval during which strong solar or nebular fields were present (Schubert et al. 1988). Permanent magnetization from an internal source has been questioned on the grounds that a high specific magnetization of the shell and a characteristic interval between field reversals much longer than on Earth are both required (Schubert et al. 1988).

The hypothesis that Mercury's internal field is remanent received renewed attention after the discovery of strongly magnetized regions in the crust of Mars (Acuña et al. 1999). Mars may not be a good analogue to Mercury in all respects, because the potential magnetic carriers on Mars are iron-rich oxides (Kletetschka et al. 2000) and, as discussed earlier, Mercury's crust appears to be very low in Fe^{2+}. The possibility remains, however, that Mercury's crust may contain sufficient metallic iron or iron sulfides (Sprague et al. 1995) to display magnetic thermoremanence and crustal fields detectable from orbit.

A fresh look at the idea that crustal remanence may give rise to the dipolar field has come from a consideration of the strong variation of solar heating with latitude and longitude on Mercury (Aharonson et al. 2004). Because Mercury's obliquity is small, equatorial regions are heated by the Sun to a greater degree than polar regions. Further, Mercury's eccentric orbit and 3 : 2 spin–orbit resonance result in two equatorial "hot poles" that view the Sun at zenith when Mercury is at perihelion (and two equatorial "cold poles" midway between them). Despite a theorem that a uniform spherical shell magnetized by an internal field displays no external field after the internal field has been removed (Runcorn 1975), a result that is not strictly correct when the magnetizing effect of the crustal field is included (Lesur and Jackson 2000), the thickness of Mercury's crust that is below the Curie temperature of a given magnetic carrier varies spatially (Aharonson et al. 2004). As a result, there is a strong dipolar contribution to the external field that would be produced by a crust magnetized by a past internal field, the predicted dipole moment (Aharonson et al. 2004) is within the range

of estimates for Mercury (Connerney and Ness 1988), and the predicted ratio of quadrupole to dipole terms (Aharonson et al. 2004) is testable with spacecraft measurements.

A challenge to the hypothesis that Mercury's magnetic field is the product of a hydromagnetic dynamo in a liquid, metallic outer core is that the field is comparatively weak. At a dipole moment three orders of magnitude less than Earth's (Connerney and Ness 1988), Mercury's field is difficult to reconcile with the common expectation for dynamos that Lorentz and Coriolis forces in the outer core are comparable in magnitude (Stevenson 2003), a condition known as magnetostrophic balance. Explanations for the weak external field involving a dynamo otherwise broadly similar to Earth's include thin-shell (Stanley et al. 2005) and thick-shell (Heimpel et al. 2005) dynamos for which a comparatively strong toroidal field maintains magnetostrophic balance and a dynamo that operates only deep in a fluid outer core beneath an electrically conductive but stable layer of liquid metal (Christensen 2006). For the first class of models, strong radial magnetic flux patches outside the cylinder aligned with the spin axis and tangent to the inner core should be found at different latitudes for the thin-shell and thick-shell models (Zuber et al. 2007), and for the latter model the multipolar expansion of external field strength is predicted to have little energy beyond the quadrupole term (Christensen 2006), so there are clear tests of these models that can be made from orbital magnetic field measurements.

A hydromagnetic dynamo as an explanation for Mercury's field (Schubert et al. 1988; Stevenson 2003) requires both that a substantial fraction of Mercury's core is presently fluid and that there are sufficient sustained sources of heat or chemical buoyancy within the core to drive the convective motions needed to maintain a dynamo. Because it is not known that either requirement is met in Mercury, and because of Mercury's weak field strength, more exotic dynamo models have also been considered. If the fluid outer core is sufficiently thin and the core–mantle boundary is distorted by mantle convective patterns, thermoelectric currents might be driven by temperature differences at the top of the core (Stevenson 1987; Giampieri and Balogh 2002). A thermoelectric dynamo is likely to produce a field richer in shorter wavelength harmonics than an Earth-like dynamo (Stevenson 1987), and these harmonics may correlate with those for the gravity field (Giampieri and Balogh 2002), so testing for such a dynamo should be possible from orbital measurements.

The presence of significant heat production within the core would expand the range of conditions under which a modern core dynamo would be expected. New laboratory experiments have reopened the question of whether a significant fraction of potassium in a differentiating terrestrial planet may partition into a liquid metal phase at high pressures (Murthy et al. 2003). Although potassium is not expected to be abundant on Mercury on the basis of several of the cosmochemical hypotheses for the planet's high metal fraction, potassium derived from surface materials is present in the atmosphere and even a small fraction of ^{40}K in the core could have a pronounced impact on the history of core cooling and the energy available to maintain a core dynamo. Tidal dissipation in the outer core may be important for maintaining a fluid state, but uncertainties in Mercury's internal structure prevent a definitive assessment (Bills 2002).

As a result of Mercury's small dipole moment, the planet's magnetosphere (Fig. 5) is among the smallest in the solar system and stands off the solar wind only 1,000–2,000 km above the surface (Slavin et al. 2007). Although the magnetosphere shares many features with that of Earth, because of its small size the timescales for wave propagation and convective transport are much shorter at Mercury, and the proximity to the Sun renders the driving forces more intense. Strong variations in magnetic field and energetic particle characteristics observed by Mariner 10 have been interpreted as evidence of magnetic substorms and magnetic reconnection in the tail (Siscoe and Christopher 1975;

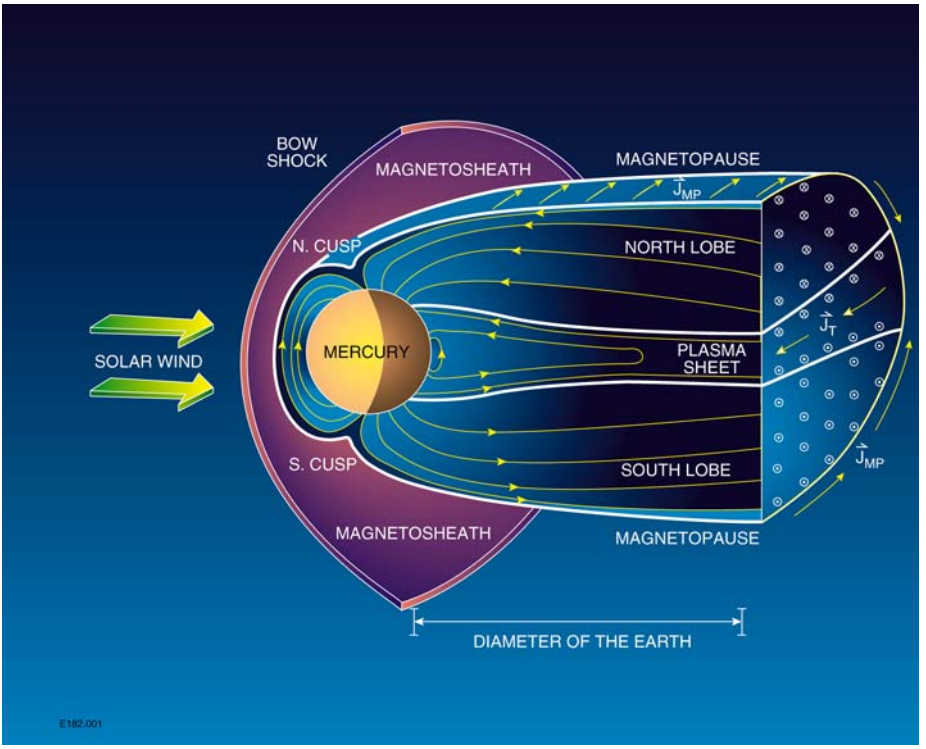

Fig. 5 A simplified, schematic view of Mercury's magnetic field and magnetosphere consistent with Mariner 10 observations and scaling of analogous features from the Earth's magnetosphere. Not depicted are the expected intense temporal variations in magnetospheric characteristics and dynamics and the consequent strong interactions among the solar wind, magnetosphere, exosphere, surface regolith, and planetary interior. From Slavin (2004)

Baker et al. 1986; Eraker and Simpson 1986; Christon 1987). The absence of a significant conducting ionosphere at Mercury, however, implies that the associated current systems close in Mercury's regolith (Janhunen and Kallio 2004) or through a process of pick-up ion formation (Cheng et al. 1987). Magnetic reconnection at the dayside magnetopause may erode the subsolar magnetosphere and allow solar wind ions to impact the planetary surface, but induced currents in Mercury's interior may act to resist magnetospheric compression (Hood and Schubert 1979). All of these factors are expected to lead to complex interactions among the solar wind, magnetosphere, exosphere, regolith, and interior (Slavin et al. 2007).

Determining the geometry of Mercury's intrinsic magnetic field and the structure of Mercury's magnetosphere will elucidate all of these issues. A challenge to the determination of the internal field, however, is that external sources can dominate the total measured field, as was the situation for Mariner 10 (Ness et al. 1976). Errors from external fields were such that the uncertainty in Mercury's dipole moment derived from Mariner 10 data is a factor of 2, and higher order terms are linearly dependent (Connerney and Ness 1988). Simulations of field recovery from orbital observations to be made by MESSENGER (Korth et al. 2004), however, indicate that the effects of the dynamics of the solar wind and Mercury's magnetosphere can be substantially reduced and important aspects of the internal field determined.

3.4 What Are the Structure and State of Mercury's Core?

An observation that can demonstrate the existence and determine the radius of a liquid outer core on Mercury (Fig. 2) is the measurement of the amplitude of Mercury's forced physical libration (Peale 1988). The physical libration of the mantle (manifested as an annual variation in the spin rate about the mean value) is the result of the periodically reversing torque on the planet as Mercury rotates relative to the Sun. The amplitude of this libration ϕ_0 is approximately equal to $(B - A)/C_m$, where A and B are the two equatorial principal moments of inertia of the planet and C_m is the polar moment of inertia of the solid outer part of the planet (Peale 1988). The moment differences also appear in expressions for the second-degree coefficients of the planetary gravity field expanded in spherical harmonics. The latter relations, the libration amplitude, and an expression resulting from Mercury's resonant state and relating the planet's small but non-zero obliquity to moment differences and other orbital parameters together yield C_m/C, where C is the polar moment of inertia of the planet (Peale 1988). The quantity C_m/C is unity for a completely solid planet and about 0.5 if Mercury has a fluid outer core (Peale 1988).

Two conditions on the above relationship for ϕ_0 are that the fluid outer core does not follow the 88-day physical libration of the mantle and that the core does follow the mantle on the timescale of the 250,000-year precession of the spin axis (Peale 1988). These constraints lead to bounds on the viscosity of outer core material, under the assumption that coupling between the outer core and solid mantle is viscous in nature, but the bounds are so broad as to be readily satisfied. Alternative core–mantle coupling mechanisms, including pressure forces on irregularities in the core–mantle boundary, gravitational torques between the mantle and an axially asymmetric solid inner core, and magnetic coupling between the electrically conductive outer core and a conducting layer at the base of the mantle, do not violate either of the required conditions (Peale et al. 2002; Zuber et al. 2007).

Of the four quantities needed to determine whether Mercury has a fluid outer core, two of them—the second-degree coefficients in the planet's gravitational field—can be determined only by tracking a spacecraft near the planet (Anderson et al. 1987). Two means for determining the remaining two quantities—the obliquity and the forced libration amplitude—from a single orbiting spacecraft have been proposed. One makes use of imaging from a spacecraft with precise pointing knowledge (Wu et al. 1997), while the other involves repeated sampling of the global topography and gravity fields (Smith et al. 2001). The MESSENGER mission will use the latter approach (Zuber et al. 2007). Mercury's obliquity and libration amplitude can also be determined from Earth-based radar observations, using either multiple images of features on Mercury viewed with a common geometry but at differing times (Slade et al. 2001) or correlations of the speckle pattern in radar images of the planet obtained at two widely separated antennas (Holin 2002). Observations made with the latter method indicate that $C_m/C < 1$ at 95% confidence (Margot et al. 2007), a result strongly indicative of a molten outer core. Improved estimates of C_m/C as well as the determination of C require a more precise determination of the planetary gravity field from tracking an orbiting spacecraft.

3.5 What Are the Radar-Reflective Materials at Mercury's Poles?

The discovery in 1991 of radar-bright regions near Mercury's poles and the similarity of the radar reflectivity and polarization characteristics of these regions to those of icy satellites and the south residual polar cap of Mars led to the proposal that these areas host deposits of

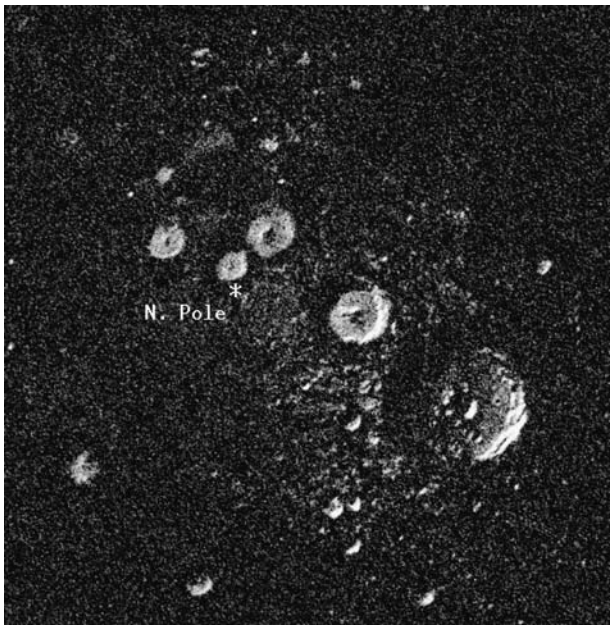

Fig. 6 Radar image of the north polar region of Mercury, obtained by the Arecibo Observatory in July 1999 (Harmon et al. 2001). The radar illumination direction is from the upper left, and the resolution is 1.5 km. Mercury polar deposits are the radar-bright regions within crater floors

surface or near-surface water ice (Harmon and Slade 1992; Slade et al. 1992). Subsequent radar imaging at improved resolution (Fig. 6) has confirmed that the radar-bright deposits are confined to the floors of near-polar impact craters (Harmon et al. 2001). Because of the small obliquity of the planet, sufficiently deep craters are permanently shadowed and are predicted to be at temperatures at which water ice is stable for billions of years (Paige et al. 1992). Such water ice is not likely to represent exposed portions of larger subsurface polar caps, on the grounds that polar craters display depth-to-diameter ratios similar to those of equatorial craters, contrary to the terrain softening expected in areas of subsurface ice (Barlow et al. 1999). While a contribution from interior outgassing cannot be excluded, impact volatilization of cometary and meteoritic material followed by random-walk transport of water molecules to polar craters can provide sufficient polar ice to match the characteristics of the deposits (Moses et al. 1999).

The highest-resolution images of polar deposits show that they extend more than 10° in latitude from the pole and that for larger craters farther from the pole the radar-bright material is concentrated on the side of the crater floor farthest from the pole (Harmon et al. 2001). Both of these characteristics are consistent with thermal models for water ice insulated by burial beneath a layer of regolith tens of centimeters thick (Vasavada et al. 1999), although the detection of radar-bright features in craters as small as 10 km in diameter and the observation that some radar-bright deposits within about 30° of longitude from the equatorial "cold poles" extend up to 18° southward from the pole pose difficulties for current thermal models (Harmon et al. 2001).

Two alternative explanations of the radar-bright polar deposits of Mercury have been suggested. One is that the polar deposits are composed of elemental sulfur rather than water ice, on the grounds that sulfur would be stable in polar cold traps and the presence of sulfides in the regolith can account for a high disk-averaged index of refraction and low microwave opacity of surface materials (Sprague et al. 1995). The second alternative hypothesis is that the permanently shadowed portions of polar craters are radar bright not because of trapped

volatiles but because of either unusual surface roughness (Weidenschilling 1998) or low dielectric loss (Starukhina 2001) of near-surface silicates at extremely cold temperatures. This second suggestion can be tested by carrying out impact experiments with very cold silicate targets (Weidenschilling 1998) or measuring dielectric losses of silicates at appropriate temperatures and frequencies (Starukhina 2001), while the first proposal can potentially be tested by measurements from an orbiting spacecraft.

Determining the nature of the polar deposits from Mercury orbit will pose a challenge because the deposits will occupy a comparatively small fraction of the viewing area for most remote sensing instruments (Boynton et al. 2007) and because any polar volatiles may be buried beneath a thin layer of regolith (Vasavada et al. 1999). The most promising measurements include searches of the polar atmosphere with an ultraviolet spectrometer for the signature of excess OH or S (Killen et al. 1997) and neutron spectrometer observations of the polar surface to seek evidence for near-surface hydrogen (Feldman et al. 1997).

3.6 What Are the Important Volatile Species and Their Sources and Sinks on and near Mercury?

Mercury's atmosphere is a surface-bounded exosphere whose composition and behavior are controlled by interactions with the magnetosphere and the surface (Domingue et al. 2007). The exosphere is known to contain six elements (H, He, O, Na, K, Ca). The Mariner 10 airglow spectrometer detected H, He, and O (Broadfoot et al. 1974, 1976), while ground-based spectroscopic observations led to the discovery of Na (Potter and Morgan 1985), K (Potter and Morgan 1986), and Ca (Bida et al. 2000). The exosphere is not stable on timescales comparable to the age of the planet (Hunten et al. 1988), so there must be sources for each of the constituents. H and He are likely to be dominated by solar wind ions neutralized by recombination at the surface, but the other species are likely derived from impact vaporization of micrometeoroids hitting Mercury's surface or directly from Mercury surface materials (Domingue et al. 2007).

Proposed source processes for supplying exospheric species from Mercury's crust include diffusion from the interior, evaporation, sputtering by photons and energetic ions, chemical sputtering by protons, and meteoritic infall and vaporization (Killen et al. 1999). That several of these processes play some role is suggested by the strong variations in exospheric characteristics observed as functions of local time, solar distance, and level of solar activity (Potter et al. 1999; Killen et al. 2001; Hunten and Sprague 2002) as well as by correlations between atmospheric Na and K enhancements and surface features (Sprague et al. 1998). Simulations of Mercury's Na exosphere and its temporal variation in which most of the above source processes are incorporated have shown that evaporation exerts a strong control on the variation of surface Na with time of day and latitude (Leblanc and Johnson 2003). These simulations provide good matches to measurements of changes in the Na exosphere with solar distance and time of day (Sprague et al. 1997) and observations (Potter et al. 2002b) of Mercury's sodium tail (Fig. 7).

The presence of the volatile elements Na and K in Mercury's exosphere poses a potential challenge for the hypotheses advanced to account for Mercury's high ratio of metal to silicate. Whether Mercury is metal rich because of mechanical segregation between metal and silicate grains in the hot, inner solar nebula (Weidenschilling 1978) or because of extensive volatilization or impact removal of the outer portions of a differentiated planet (Cameron 1985; Fegley and Cameron 1987; Benz et al. 1988; Wetherill 1988), the planetary crustal concentrations of volatile elements should be very low. For several of the proposed sources of exospheric Na and K, surface abundances ranging from a few tenths of a percent to a few

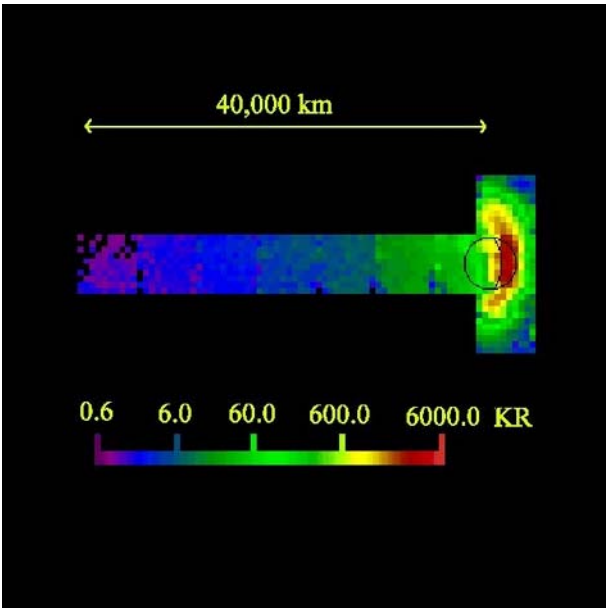

Fig. 7 Composite image of the sodium D2 emission line in the vicinity of Mercury obtained at the McMath-Pierce Solar Telescope at the National Solar Observatory on May 26, 2001 (Potter et al. 2002a). The Na tail is in the anti-sunward direction, and south is at the top. The *color scale* for intensity (in kiloRayleighs) is logarithmic

percent by weight are commonly required (Killen et al. 2001). Simulations of variations in the exospheric Na abundance, however, can match all observations with a supply of fresh Na no greater than that predicted by meteoritic impact volatilization (Leblanc and Johnson 2003).

A spacecraft in orbit about Mercury will provide a range of opportunities for elucidating further the nature of the exosphere. Limb scans conducted with an ultraviolet–visible spectrometer can monitor variations in the major exospheric constituents and search for new species. Surface sources of exospheric materials can be mapped with gamma-ray, X-ray, and neutron spectrometers. Measurement of energetic and thermal plasma ions will detect solar-wind pick-up ions that originated as exospheric neutral atoms.

4 Mission Science and Measurement Objectives

The six guiding science questions lead naturally to six science objectives for the MESSENGER mission, which in turn lead to corresponding sets of measurement objectives to be accomplished by the spacecraft (Fig. 8).

Addressing the origin of Mercury's anomalously high ratio of metal to silicate leads to the scientific objective to map globally the major element chemistry and mineralogy of the planet's surface. To differentiate among the leading formation hypotheses for Mercury, the elements mapped should include both volatile (e.g., K) and refractory (e.g., Ca, Al) species. Spectral measurements from visible to near-infrared wavelengths at spatial resolutions of several kilometers or better are needed to search for absorption features diagnostic of mineralogy. The global maps should at least regionally be at a resolution sufficient to distinguish the compositions of the principal geological units and to determine whether the composition of material excavated from depth and ejected by young impact craters differs from that of surrounding surface materials (cf. Blewett et al. 2007). MESSENGER will obtain major-

Guiding Questions	Science Objectives	Measurement Objectives
What planetary formational processes led to the high ratio of metal to silicate in Mercury?	Map the elemental and mineralogical composition of Mercury's surface	Surface elemental abundances: GRNS and XRS Spectral measurements of surface: MASCS (VIRS)
What is the geological history of Mercury?	Image globally the surface at a resolution of hundreds of meters or better	Global imaging in color: MDIS (WAC) Targeted high-resolution imaging: MDIS (NAC) Global stereo: MDIS Spectral measurements of geological units: MASCS (VIRS) Northern hemisphere topography: MLA
What are the nature and origin of Mercury's magnetic field?	Determine the structure of the planet's magnetic field	Mapping of the internal field: MAG Magnetospheric structure: MAG, EPPS
What are the structure and state of Mercury's core?	Measure the libration amplitude and gravitational field structure	Gravity field, global topography, obliquity, libration amplitude: MLA, RS
What are the radar reflective materials at Mercury's poles?	Determine the composition of the radar-reflective materials at Mercury's poles	Composition of polar deposits: GRNS Polar exosphere: MASCS (UVVS) Polar ionized species: EPPS Altimetry of polar craters: MLA
What are the important volatile species and their sources and sinks on and near Mercury?	Characterize exosphere neutrals and accelerated magnetosphere ions	Neutral species in exosphere: MASCS (UVVS) Ionized species in magnetosphere: EPPS Solar wind pick-up ions: EPPS Elemental abundances of surface sources: GRNS, XRS

Fig. 8 The guiding questions, science objectives, and measurement objectives for the MESSENGER mission. Each question will be answered by observations from two or more elements of the MESSENGER payload, and the observations from each instrument will address multiple questions

element maps of Mercury's surface at 10% relative uncertainty or better at the 1,000-km scale and determine local composition and mineralogy at the ∼20-km scale.

Assessing the geological history of Mercury leads to the scientific objective to image globally the planetary surface at a horizontal resolution of hundreds of meters or better coupled with spectral measurements of major geologic units at visible and near-infrared wavelengths. Viewing geometry for imaging should be optimized to discern geological features over a range of scales. High-resolution imaging and the determination of topographic profiles across key geological features from altimetry or stereo will aid in the interpretation of surface geological processes. MESSENGER will obtain a global image mosaic (monochrome) with at least 90% coverage at 250-m average resolution or better, image at least 80% of the planet stereoscopically, obtain a global multi-spectral map at 2 km/pixel average resolution or better, and map the topography of the northern hemisphere at a 1.5-m average height resolution.

Addressing the nature and origin of Mercury's internal magnetic field leads to a requirement to make measurements of the vector magnetic field both near the planet and throughout the planet's magnetosphere. Repeated measurements from orbit are needed to separate internal from external contributions to the field. Measurement of the distributions of energetic particles and plasma boundaries will be critical in the interpretation of magnetospheric structure and dynamics and their relationship to the internal field and solar wind conditions. MESSENGER will obtain a multipole model of Mercury's internal magnetic field resolved through quadrupole terms with an uncertainty of less than ∼20% in the dipole magnitude and direction.

Determining the size of Mercury's core and whether its outer core is liquid or solid requires the measurement of Mercury's obliquity, the amplitude of Mercury's physical libration, and the magnitude of the second-degree coefficients in the harmonic expansion of Mercury's gravitational field. These quantities can be measured by repeated altimetric measurements of Mercury's long-wavelength shape and by the determination of Mercury's gravitational field from ranging and range-rate measurements from an orbiting spacecraft. MESSENGER will provide a global gravity field to spherical harmonic degree and order 16 and determine the ratio of the polar moment of inertia of the solid outer shell of the planet to the polar moment of inertia of the entire planet (C_m/C) to ∼20% or better.

Determining the nature of Mercury's polar deposits is a challenging goal for a spacecraft in an orbit that does not feature a low-altitude periapsis over one of the poles, but several measurements are promising. Ultraviolet spectrometry of Mercury's near-limb region can reveal whether species diagnostic of candidate polar deposit materials (e.g., OH, S) are present at excess levels in the polar exosphere. Gamma-ray and neutron spectrometry, for sufficiently strong signals, could detect an enhancement of near-surface H in the floors of polar craters. Imaging and altimetry of high-latitude craters can confirm which areas are in permanent shadow and strengthen thermal models for polar regions. By use of all of these methods, MESSENGER aims to identify the principal component the polar deposits at Mercury's north pole.

Determining the volatile budget on Mercury and the sources and sinks for dynamic variations in the exosphere leads to measurement requirements for the identification of all major neutral species in the exosphere and all major charged species in the magnetosphere. The former can be accomplished by ultraviolet and visible wavelength spectrometry of the exosphere with sufficient spectral resolution to detect and identify emission lines diagnostic of known and possible species. The latter can be carried out by in situ analysis of the energies and compositions of charged particles within and in the vicinity of Mercury's magnetosphere. Measurements of surface composition will illuminate the question of

the extent to which surface materials act as sources for the exosphere, and measurements of magnetosphere-solar wind interactions will inform questions on the sources and sinks of magnetospheric and exospheric species. MESSENGER will obtain altitude profiles at 25-km resolution of the major neutral exospheric species and characterize the energy distributions of major ion species, both as functions of local time, Mercury heliocentric distance, and solar activity.

5 Payload Overview

The measurement objectives for MESSENGER (Fig. 8) are met by a payload consisting of seven instruments plus radio science. The instruments (Fig. 9) include the Mercury Dual Imaging System (MDIS), the Gamma-Ray and Neutron Spectrometer (GRNS), the X-Ray Spectrometer (XRS), the Magnetometer (MAG), the Mercury Laser Altimeter (MLA), the Mercury Atmospheric and Surface Composition Spectrometer (MASCS), and the Energetic Particle and Plasma Spectrometer (EPPS). The instruments communicate to the spacecraft through fully redundant Data Processing Units (DPUs). The mass and power usage of each instrument are listed in Table 1. A brief summary of each of the seven instruments is given below. This summary updates an overview of the payload published early in the design stage of the project (Gold et al. 2001). Detailed descriptions of each instrument can be found in companion papers in this volume (Anderson et al. 2007; Andrews et al. 2007; Cavanaugh et al. 2007; Goldsten et al. 2007; Hawkins et al. 2007; McClintock and Lankton 2007; Schlemm et al. 2007). The MESSENGER radio science (RS) capabilities and objectives are described in another companion paper (Srinivasan et al. 2007).

5.1 MDIS

The MDIS instrument (Hawkins et al. 2007) includes both a wide-angle camera (WAC) and a narrow-angle camera (NAC) with an onboard pixel summing capability. That combi-

Table 1 Some characteristics of MESSENGER instruments

Instrument	Mass[a] (kg)	Power[b] (W)
MDIS	8.0	7.6
GRNS	13.1	22.5
XRS	3.4	6.9
MAG	4.4	4.2
MLA	7.4	16.4
MASCS	3.1	6.7
EPPS	3.1	7.8
DPUs	3.1	12.3
Miscellaneous[c]	1.7	
Total	47.2	84.4

[a] Mass includes mounting hardware and captive thermal control components. The mass for MDIS includes the calibration target. The MAG mass includes the boom

[b] Nominal average power consumption per orbit; actual values will vary with instrument operational mode and spacecraft position in orbit

[c] Includes purge system, payload harnesses, and magnetic shielding for the spacecraft reaction wheels

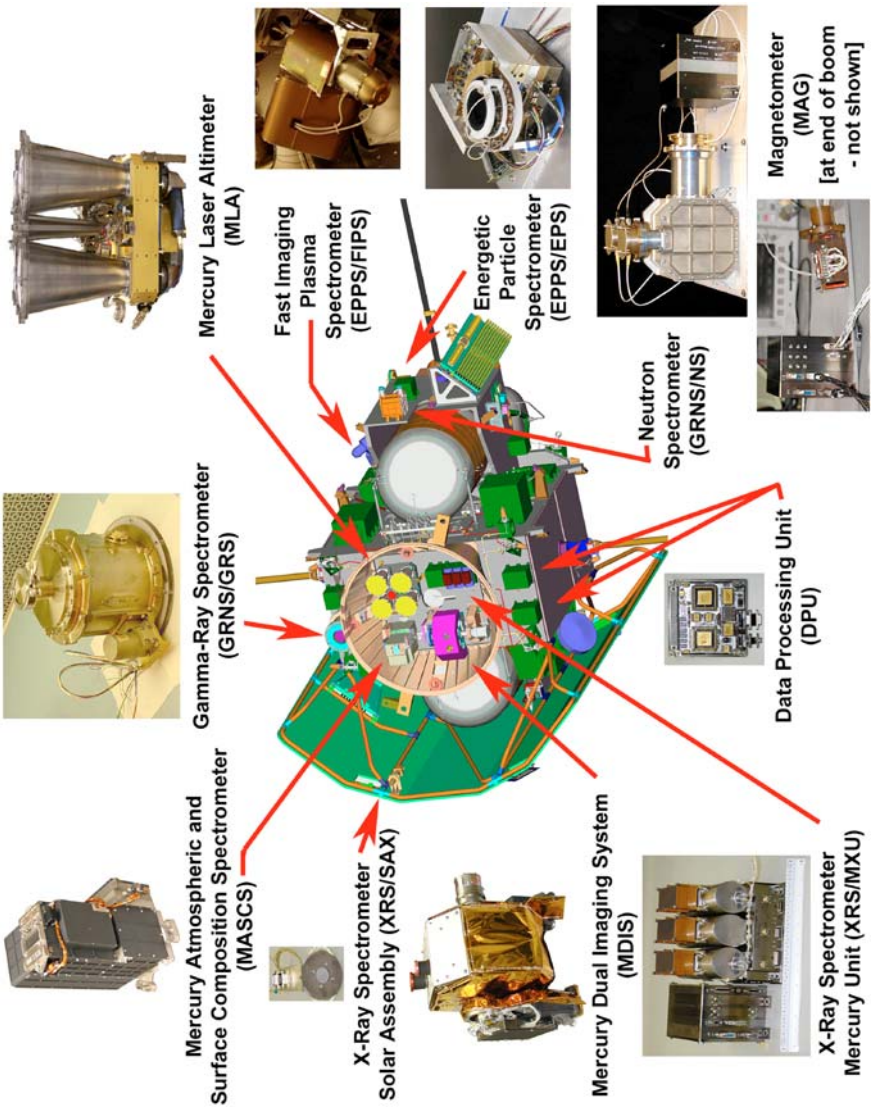

Fig. 9 MESSENGER payload instruments and their locations on the spacecraft. The Magnetometer is mounted at the end of a 3.6-m boom (not shown) that extends in the anti-sunward direction. The Solar Assembly for X-rays (SAX) is mounted on the Sun-facing side of the spacecraft's sunshade (Leary et al. 2007)

nation of features was chosen to provide images of a nearly uniform horizontal resolution throughout MESSENGER's elliptical orbit while minimizing downlink requirements. Because of the geometry of the orbit and limitations on off-Sun pointing by the spacecraft, the WAC and NAC are mounted on opposite sides of a pivoting platform to provide for optical navigation and planetary mapping during the Mercury flybys. MDIS is the only MESSENGER instrument with a pointing capability independent of the spacecraft attitude. The MDIS pivot can point from 50° toward the Sun to 40° anti-sunward centered on nadir, where it is co-aligned with the other optical instruments, all of which are mounted on the spacecraft lower deck (Fig. 9). The pivot platform drive has a redundant-winding stepper motor system and a resolver to measure the platform rotation to a precision <75 μrad.

The thermal design for MDIS faced the challenge that the instrument must work in cold space and yet be able to point at the >700-K sub-solar region of Mercury for extended periods and still produce high-quality images. Throughout this range of environmental conditions, the charge-coupled device (CCD) camera heads are maintained between -10 and -40°C to minimize their dark noise. The MDIS thermal protection system includes high-heat-capacity beryllium radiators, diode heat pipes to shut off thermal conduction when viewing the hot planet, phase-change "wax packs" to limit temperatures during hot periods, and flexible thermal links to tie these elements together.

The WAC is a refractive design with a 10.5° field of view (FOV) and a 12-position filter wheel to provide full-color mapping. The NAC is an off-axis reflective design with a 1.5° FOV and a single band-limiting filter. The passband is a compromise between limiting the light at Mercury to keep the exposure times reasonable and providing high throughput for stellar imaging required for optical navigation.

The CCD camera heads use highly integrated, low-mass electronics with 12-bit intensity resolution. The CCD detectors are 1,024 × 1,024 pixel frame-transfer devices with electronic shuttering. There is no mechanical shutter. There are both manual and automatic exposure controls, and the exposure range is from 1 ms to ∼10 s. The cameras can be commanded to perform on-chip summing of 2 × 2 pixels for 512 × 512 pixel images as required. The imager hardware can also compress the images from 12-bit to 8-bit quantization with a variety of look-up tables. Images are sent directly to the spacecraft solid-state recorder. They are later read back into the main spacecraft processor for additional image compression as commanded on an image-by-image basis.

5.2 GRNS

The GRNS instrument (Goldsten et al. 2007) includes two sensors, a Gamma-Ray Spectrometer (GRS) and a Neutron Spectrometer (NS). The GRS is a cryocooled, high-purity germanium detector with an active shield and measures elemental abundances of O, Si, S, Fe, H, K, Th, and U. Because it was not practical to mount the GRS on a long boom in the Mercury thermal environment, the signal-to-background ratio was maximized by choice of detector. Developing an actively cooled detector to operate at <90 K in the >700 K environment at Mercury was a significant design challenge. The GRS sensor has a 50 × 50 mm cylindrical detector with a Stirling-cycle cooler and an active scintillator shield of boron-loaded plastic. A triple-layer thermal shield surrounds the germanium detector to minimize heat leaks. The boron-loaded plastic scintillator shield is viewed by a large photomultiplier tube (PMT). The anti-coincidence shield removes the cosmic-ray background and softer component of the spacecraft gamma-ray background. The boron loading in the shield also responds directly to slow neutrons and thereby supplements the NS data. The GRS electronics use a novel signal processing design that achieves linearity and stability that nearly

equal the performance of a full digital signal processing system with a minimal amount of radiation-hardened electronics.

The NS part of the GRNS is particularly sensitive to the presence of H but may also provide information on Fe content. The NS sensor has two lithium glass scintillators on the ends separated by a beveled cube of neutron-absorbing, borated plastic scintillator. The glass scintillator plates are loaded with lithium enriched in ^{6}Li to detect thermal and epithermal neutrons. Because the MESSENGER orbital velocity is about 3 km/s, the difference in counts in the ram and wake directions greatly enhances the discrimination of thermal and epithermal neutrons. The borated-plastic central scintillator counts epithermal neutrons from all directions and measures the energy depositions of fast neutrons. All three scintillators are viewed by individual PMTs.

5.3 XRS

XRS is an improved version of the Near Earth Asteroid Rendezvous (NEAR) Shoemaker X-ray spectrometer to measure the atomic surface abundances of Mg, Al, Si, Ca, Ti, and Fe by solar-induced X-ray fluorescence (Schlemm et al. 2007). Three gas proportional counters measure low-energy X-rays from the planet, and a Si-PIN detector mounted on the spacecraft sunshade (Fig. 9) views the solar X-ray input. The detectors cover the energy range from 1 to 10 keV. XRS proportional counters have a 12° FOV, provided by a high-throughput, Cu–Be honeycomb collimator. A matched filter technique is used to separate the lower energy X-ray lines (Al, Mg, and Si). The proportional counter tubes are improved from the NEAR Shoemaker design by the addition of anticoincidence wires surrounding most of the tube, a low-emission carbon liner in the sensitive volume, and field-equalizing structures at the ends of the tube to prevent the charge build-up that was seen on that spacecraft. The planet-viewing portion of the instrument, the Mercury X-ray Unit (MXU) is mounted on the lower spacecraft deck (Fig. 9). The XRS solar monitor consists of a small (0.03 mm^2 aperture) detector protected by a pair of thin Be foils. The outer foil reaches >500°C and is the hottest component on the spacecraft, while the detector, just 4 cm away, sits at −45°C.

5.4 MAG

MAG is a three-axis, ring-core, fluxgate magnetometer of the same basic design as that flown on many planetary missions (Anderson et al. 2007). The MAG sensor head is mounted on a lightweight, 3.6-m carbon-fiber boom extending in the anti-sunward direction. Because the sensor can protrude from the shadow of the spacecraft when the spacecraft is pointed near its allowable off-Sun limits, the sensor has its own sunshade. The MAG detector samples the field at a 20-Hz rate, and hardware anti-aliasing filters plus software digital filters provide selectable readout intervals from 0.05 s to 100 s. Readout intervals greater than 1 s generate a sample of the 0.5-Hz filtered signal at the time of the readout. MAG data are output with 16-bit quantization, which eliminates the need for range switching during orbital operations at the ±1530-nT full-scale range. Auto-ranging is provided at the less sensitive range, ±51,300 nT full scale, in the event that large crustal fields are present. Spacecraft-induced stray fields were minimized during subsystem development and fabrication. The reaction wheels and a few propulsion system valves were provided with shielding and compensation magnets, respectively, as needed to meet requirements on background magnetic fields.

5.5 MLA

MLA includes a diode-pumped, Q-switched, Cr:Nd:YAG laser transmitter operating at 1,064 nm wavelength and four receiver telescopes with sapphire lenses (Cavanaugh et al. 2007). MLA is mounted on the spacecraft lower deck (Fig. 9), along with the other optical instruments. A silicon avalanche photodiode (APD) and a time-interval unit, based on an application-specific integrated circuit (ASIC) chip, measure altitudes to 30-cm precision or better and ranges up to 1,200 km. Because of MESSENGER's elliptical orbit at Mercury, MLA will operate for about 30 minutes around the periapsis of each orbit. The laser transmits pulses at 8 Hz through a beam expander with a heat-absorbing sapphire window. The four 115-mm-diameter receiver telescopes comprise a multi-aperture receiver, which collects the laser return pulses from Mercury and passes them via four optical fibers through an optical bandpass filter to reject the solar background before going to the silicon APD detector.

5.6 MASCS

The MASCS instrument combines an exospheric and a surface-viewing instrument in a single package (McClintock and Lankton 2007). A moving-grating Ultraviolet-Visible Spectrometer (UVVS) will observe emissions from the Mercury exosphere during limb scans, and a Visible-Infrared Spectrograph (VIRS) will observe the planetary surface. The two spectrometers are contained in the same package and fed by a single front-end telescope. The Cassegrain telescope feeds the UVVS Ebert-Fastie spectrometer directly. Its moving diffraction grating design is optimized for measuring the very weak emissions of the exosphere with excellent signal-to-noise ratio. UVVS spans the spectral range from 115 to 600 nm with three photon-counting PMT detectors. When scanning the limb, it has 25-km altitude resolution and an average spectral resolution of 1 nm. VIRS is fed by a fused-silica fiber-optic bundle from the focal plane of the front-end telescope. A holographic diffraction grating images onto two semiconductor line-array detectors. A dichroic beam splitter separates the visible (300–1,025 nm) and infrared (0.95–1.45 μm) spectra. The 512-element visible detector is silicon, and the 256-element infrared detector is made of InGaAs. MASCS requires no active cooling. The instrument is mounted on the lower spacecraft deck (Fig. 9).

5.7 EPPS

The EPPS (Andrews et al. 2007) instrument consists of an Energetic Particle Spectrometer (EPS) and a Fast Imaging Plasma Spectrometer (FIPS). FIPS measures thermal and low-energy ions with a unique electrostatic analyzer and a time-of-flight (TOF) spectrometer section. The FIPS analyzer is sensitive to ions entering over nearly a full hemisphere, with energy per charge (E/q) up to >15 keV/q. Particles of a given E/q and polar angle pass through the dome-shaped electrostatic deflection system and into the position-sensing TOF telescope. The ions are then post-accelerated by a fixed voltage before passing through a very thin ($\sim$1 μg/cm^2) carbon foil. Secondary electrons from the foil are measured with a position-sensitive detector that reads out the initial incidence angle. Mass per charge of an ion is measured by the E/q (set by the deflection voltage) and the TOF. The deflection voltage is stepped to cover the full E/q range in about one minute. The EPS sensor measures the TOF and residual energy of ions from 10 keV/nucleon to $\sim$3 MeV and electrons to 400 keV. Time-of-flight is measured from secondary electrons as the ions pass through two foils, while total energy is measured by a 24-pixel silicon detector array. The FOV, 160° by 12°,

is divided into six segments of 25° each. The EPPS common electronics process all of the TOF, energy, and position signals from both EPS and FIPS. EPS is mounted on the rear deck of the spacecraft, whereas FIPS is mounted on the side of the spacecraft (Fig. 9), where it can observe the plasma over a wide range of pitch angles.

5.8 RS

The radio frequency (RF) telecommunications system used to conduct radio science (RS) as well as communicate with the MESSENGER spacecraft (Srinivasan et al. 2007) includes two opposite-facing, high-gain phased-array antennas, two fanbeam medium-gain antennas, and four low-gain antennas. The RF signals are transmitted and received at X-band frequencies (7.2 GHz uplink, 8.4 GHz downlink) by the NASA Deep Space Network (DSN). Precise observations of the spacecraft's Doppler velocity and range assist in navigating the spacecraft and will be inverted to determine the planet's gravitational field, provide improvements to the planet's orbital ephemeris, and sharpen knowledge of the planet's rotation state, including obliquity and forced physical libration. The times of occultation of the spacecraft RF signal by the planet will be used to determine local values of Mercury's radius, of particular importance for Mercury's southern hemisphere, most of which will be out of range of the MLA instrument.

5.9 Complementarity of Instruments

As illustrated in Fig. 8, each of the mission science objectives will be addressed by at least two elements of the MESSENGER payload (including Radio Science). Mercury's elemental surface composition will be mapped by GRNS and XRS, which are complementary in their elemental sensitivity and the depth of near-surface material contributing to detected signals; mineralogical information will be obtained from the VIRS sensor on MASCS and, with much less spectral resolution, the color imaging that will be carried out by the WAC on MDIS. Mercury's geological history will primarily be derived from mosaics of MDIS images, in color and in high-resolution monochrome, but the interpretation of unit definition will be aided by spectral reflectance measurements by MASCS and the interpretation of geological features will be enhanced by information on topography measured by MLA and obtained from MDIS with stereogrammetry. Mercury's magnetic field will be mapped by MAG, while plasma and energetic particle characteristics measured by EPPS will help to define the principal magnetospheric boundaries consistent with internal field structure. The key parameters necessary to determine Mercury's core radius and the nature of the outer core can be derived independently from MLA and RS observations. The composition of polar deposits will be addressed by GRNS, MLA observations will address the topographic cold trap hypotheses, and MASCS and EPPS observations will address whether the polar regions have enhancements in neutral or ionized species that may be derived from polar deposit material. The processes governing the exosphere will be variously addressed by the UVVS sensor on MASCS, the EPPS measurements, and the chemical observations of potential surface source regions by GRNS and XRS.

Just as each science objective is met with data from multiple payload elements, each instrument addresses two or more of the guiding science questions. This dual complementarity provides for important crosschecks between sets of observations and ensures that mission science requirements can be met even in the case of problems with one of the payload instruments.

6 Spacecraft Overview

The requirements on the MESSENGER spacecraft (Santo et al. 2001) flowed directly from the science requirements (Solomon et al. 2001) and mission design (McAdams et al. 2007). The Delta II 7925H-9.5 launch vehicle was the largest available to a Discovery-class mission. This vehicle provided 1,107 kg of lift mass to achieve the necessary heliocentric orbit. This fact, coupled with the complex trajectory requiring that 599 kg (54%) of the spacecraft launch mass be propellant, limited the spacecraft dry mass—a challenging constraint for designing a fully redundant spacecraft with MESSENGER's functionality. A schematic view of the MESSENGER spacecraft, described in greater detail in a companion paper (Leary et al. 2007), is shown in Fig. 10, and an image of the spacecraft in the process of being mated to the launch vehicle is shown in Fig. 11.

The MESSENGER spacecraft structure, primarily lightweight composite material, was integrated at the outset of design with a dual-mode propulsion system. The propulsion system features state-of-the-art lightweight fuel tanks and can provide 2,250 m/s velocity change (ΔV) capability. A ceramic-cloth sunshade eliminates most of the solar input throughout the cruise and orbital phases of the mission. The spacecraft is three-axis stabilized and momentum biased to ensure Sun pointing while allowing instrument viewing by rotation about the spacecraft–Sun line. Power is provided by two specially designed 2.6-m^2 solar arrays consisting of two-thirds mirrors and one-third solar cells for thermal management. Generally passive thermal management techniques have been used on the rest of the spacecraft to minimize the required power while protecting the spacecraft from the harsh

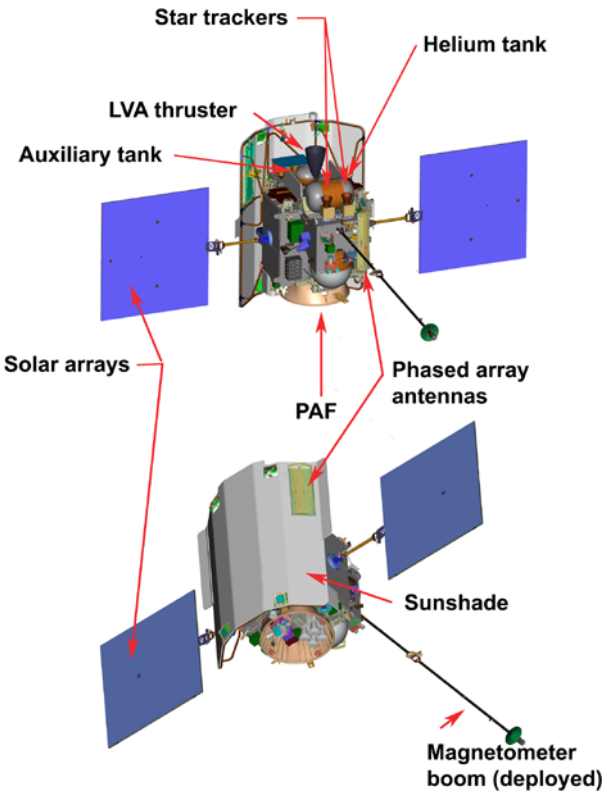

Fig. 10 Schematic view of the MESSENGER spacecraft from two perspectives. The identified tanks and the large velocity adjustment (LVA) thruster are part of the propulsion system. The payload attach fitting (PAF) mated the spacecraft to the third stage of the launch vehicle at the time MESSENGER was launched and now encloses four of the payload instruments

Fig. 11 The MESSENGER spacecraft on July 14, 2004, after it was attached to the payload assist module of the Delta II third stage at Astrotech Space Operations in Titusville, FL. The flat, reflective panels are the solar arrays stowed in their launch positions; solar cells are the dark strips between the optical solar reflectors (mirrors) that permit high-temperature operation. The gold reflective material is thermal blanket. A portion of the stowed magnetometer boom is visible between the solar arrays

environment near the Mercury dayside. A single redundant processor performs all nominal spacecraft functions, while two other processors monitor spacecraft health and safety. Telecommunications are provided by redundant transponders, solid-state power amplifiers, and a diverse antenna suite that includes two phased-array antennas, the first electronically steered antennas designed for use in deep space.

Because the spacecraft is solar powered (except for a battery needed for eclipses), power generation increases as the spacecraft moves sunward. Early in the mission the spacecraft was oriented with the sunshade pointed away from the Sun at solar distances greater than 0.85 AU, allowing a substantial reduction in needed heater power. Peak power demand occurs during science operations in orbit about Mercury. During the orbital phase, there are eclipses of varying lengths, and for the longest eclipses ($>$35 minutes) science operations are constrained by limits established to the permitted depth of discharge of the spacecraft battery.

7 Mission Timeline

MESSENGER was launched successfully by a Delta II 7925H-9.5 rocket on August 3, 2004 (Fig. 12). A summary of major mission milestones from launch to orbit insertion is given

Table 2 Key events in the MESSENGER mission

Event	Date	UTC
Launch	3 August 2004	06:15:56.5
Earth flyby	2 August 2005	19:13:08.4
DSM-1	12 December 2005	11:30:00.0
Venus flyby 1	24 October 2006	08:33:59.9
Venus flyby 2	5 June 2007	23:10:10.9
DSM-2	17 October 2007	22:30:00.0
Mercury flyby 1	14 January 2008	18:37:08.8
DSM-3	17 March 2008	19:00:00.0
Mercury flyby 2	6 October 2008	11:39:07.9
DSM-4	6 December 2008	19:00:00.0
Mercury flyby 3	29 September 2009	23:59:47.4
DSM-5	29 November 2009	19:00:00.0
MOI	18 March 2011	07:30:00.0

Times of key events are based on the full-mission reference trajectory database as of January 10, 2007. Times shown for each Deep Space Maneuver (DSM) and for Mercury Orbit Insertion (MOI) correspond to the start times of these propulsive maneuvers. Final times of future events (Venus flyby 2 and later) will differ somewhat from the values shown

in Table 2. The cruise phase of the mission is 6.6 years in duration and includes six planetary flybys—one of Earth, two of Venus, and three of Mercury—as well as a number of propulsive corrections to the trajectory (Fig. 13). At the spacecraft's fourth encounter with Mercury, orbit insertion is accomplished on March 18, 2011. A full description of the design of the MESSENGER mission and how the principal elements of mission design flowed from the science requirements is given in a companion paper (McAdams et al. 2007).

The Earth flyby was accomplished successfully on August 2, 2005, with a closest approach distance of 2,348 km over central Mongolia (McAdams et al. 2007). The event provided important calibration opportunities for four MESSENGER instruments. Prior to closest approach, MDIS acquired images of the Moon for radiometric calibration. Images of Earth (Fig. 14) were acquired with 11 filters of the MDIS wide-angle camera to test optical navigation sequences that will be used to target later planetary flybys, and a movie was assembled from 358 sets of MDIS images taken in three filters every four minutes over a 24-hour period after closest approach. MASCS obtained spectral observations of the Moon that permitted absolute radiometric calibration of UVVS and VIRS as well as intercomparison with MDIS, and MASCS observed Earth's hydrogen corona in the month following closest approach. MESSENGER also measured the magnetic field and charged particle characteristics within Earth's magnetosphere and across major magnetospheric boundaries. About two months prior to the Earth flyby, MESSENGER's MLA instrument set a distance record (24 Gm) for two-way laser transmission and detection in space (Smith et al. 2006).

The first of the two Venus flybys, which occurred on October 24, 2006, and achieved a closest approach distance of 2,987 km, increased the spacecraft's orbit inclination and reduced the orbit period. No scientific observations were made during that flyby, however, because direct communication with the spacecraft was precluded by the fact that Venus and Earth were on opposite sides of the Sun.

The second Venus flyby on June 5, 2007, will lower the spacecraft perihelion distance sufficiently to permit the subsequent three flybys of Mercury. Closest approach for the sec-

Fig. 12 Launch of the MESSENGER spacecraft on August 3, 2004. The Delta II 7925H-9.5 rocket was launched from Cape Canaveral Air Force Station Space Launch Complex 17B, Florida, at 06:15:56.5 UTC

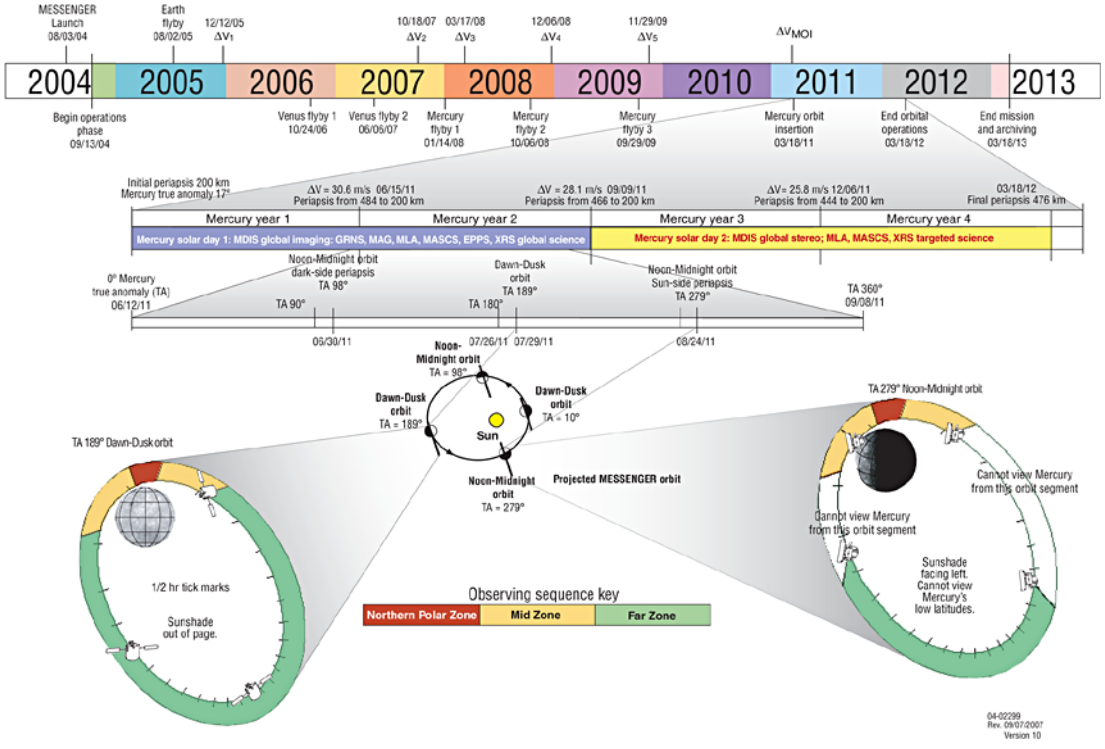

Fig. 13 The MESSENGER mission timeline. The top line shows all significant events from mission launch through end of mission and data archiving. ΔV_1 through ΔV_5 are deep-space propulsive maneuvers, and ΔV_{MOI} is the propulsive burn at Mercury orbit insertion (McAdams et al. 2007). The second line provides further details for the orbital phase of the mission. The third line expands on one Mercury year of observations, from perihelion to perihelion (0° Mercury true anomaly, or TA). The accompanying figure at the center shows the progression of the orbit in local time. Observing strategies are detailed for a dawn-dusk (terminator) orbit (TA = 189°) at lower left and a noon-midnight orbit (TA = 279°) at lower right. The divisions of these orbits by observing sequence are keyed to different data acquisition combinations for the payload instruments (Solomon et al. 2001)

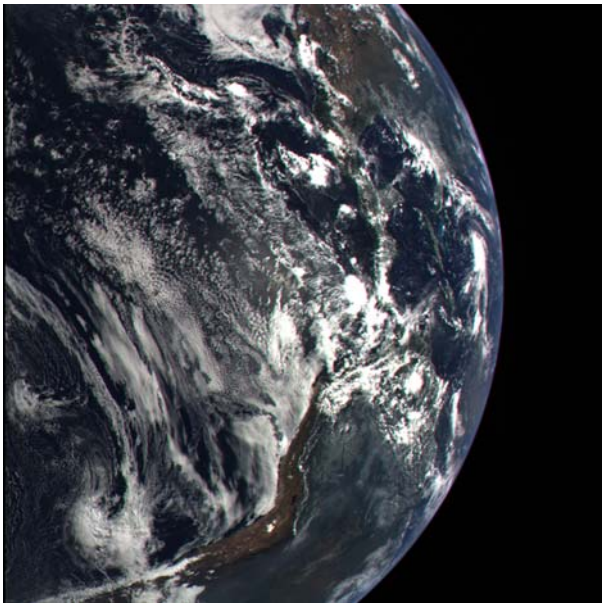

Fig. 14 MDIS WAC image of Earth taken on August 2, 2005, shortly before closest approach during the Earth flyby. Portions of North, Central, and South America are visible

ond Venus flyby is targeted at 313 km altitude over 12°S, 165°E, near the boundary between the lowlands plains of Rusalka Planitia and the rifted uplands of Aphrodite Terra. All of the MESSENGER instruments will be trained on Venus during that flyby. MDIS will image the nightside in near-infrared bands, and color and higher-resolution monochrome mosaics will be made of both the approaching and departing hemispheres. The UVVS sensor will make profiles of atmospheric species on the dayside and nightside as well as observations of the exospheric tail on departure. The VIRS sensor will observe the planet near closest approach to sense cloud chemical properties and search for near-infrared returns from the surface. The laser altimeter will serve as a passive 1,064-nm radiometer and will attempt to measure the range to one or more cloud decks for several minutes near closest approach.

The European Space Agency's Venus Express mission (Svedhem et al. 2005), now in an elliptical polar orbit about Venus, should still be operational in June 2007. The MESSENGER flyby will therefore permit the simultaneous observation of Venus from two independent spacecraft, a situation of particular value for characterization of the particle and field environment at Venus. MESSENGER's EPPS will observe charged particle acceleration at the Venus bowshock and elsewhere. The Magnetometer will provide measurements of the upstream interplanetary magnetic field (IMF), bowshock signatures, and pickup ion waves as a reference for EPPS and Venus Express observations. The encounter will enable two-point measurements of IMF penetration into the Venus ionosphere, primary plasma boundaries, and the near-tail region.

The three flybys of Mercury, in January and October 2008 and September 2009, will provide important new scientific observations of Mercury in advance of the orbital phase of the mission. MDIS will carry out an extensive campaign of imaging during each approach and departure (Solomon et al. 2001), and the geometry of the flybys (McAdams et al. 2007) are such that much of the surface unseen by Mariner 10 will have been imaged by the end of the second flyby (Hawkins et al. 2007). Each flyby will pass within 200 km of Mercury's surface, permitting measurements of the magnetic field and charged particle environment at closer distances from the planet than achieved by Mariner 10 (Connerney and Ness 1988).

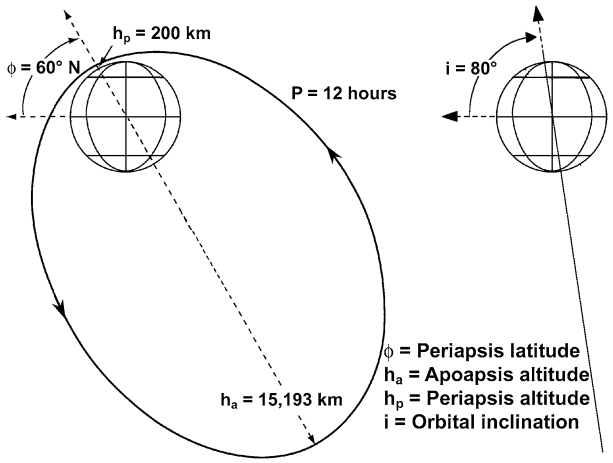

Fig. 15 MESSENGER's nominal orbit around Mercury. Parameters of the orbit were determined by balancing science objectives against propulsion and trajectory constraints and the design of the spacecraft thermal and power systems

The UVVS system on the MASCS instrument will carry out surveys of exospheric species and map the species in Mercury's magnetotail, and VIRS will conduct detailed mapping of dayside surface reflectance at visible and near-infrared wavelengths in search of mineralogical absorption features. The MLA will range to the surface near nightside closest approaches, and the GRNS and XRS instruments will collect early baseline measurements of the Mercury environment.

Within a few days of orbit insertion, the spacecraft will be in its mapping orbit, which has an 80° inclination to Mercury's equator, an initial 200-km minimum altitude over 60°N latitude, and a 12-hour orbit period (Fig. 15). As a result of solar torques, the periapsis latitude drifts northward and the minimum altitude progressively increases. Once per 88-day Mercury year the spacecraft will execute orbit correction maneuvers to return the minimum altitude to 200 km (McAdams et al. 2007). Otherwise propulsive events will be minimized to permit the recovery of Mercury's gravity field from ranging and Doppler velocity measurements (Srinivasan et al. 2007). The orbital phase of the mission is scheduled for one Earth year, or slightly longer than two Mercury solar days (Fig. 13). At the end of the nominal mission the periapsis latitude will be 72°N. Approximately one year after the last propulsive adjustment to its orbit, the spacecraft will impact Mercury's surface.

While in Mercury orbit, observations are staged by altitude and time of day so as to maximize scientific return among all scientific instruments (Fig. 13), subject to restrictions on spacecraft attitude set by the need to maintain sunshade pointing within small angular deviations in yaw and pitch of the sunward direction (Leary et al. 2007). MDIS will build on the flyby imaging to create global color and monochrome image mosaics during the first six months of the orbital phase; a global monochrome base mosaic will be obtained at 250-m/pixel or better average spatial sampling, low emission angle, and moderate incidence angle, and a global color mosaic will be obtained at a resolution of 2 km/pixel or better. Emphasis during the second six months will shift to targeted, high-resolution imaging (up to $\sim$ 20 m/pixel resolution) with the NAC and repeated mapping at a different viewing geometry to carry out global stereogrammetry (Hawkins et al. 2007). GRNS and XRS will build up observations that will yield global maps of elemental composition at resolutions that will vary with latitude, species, and (for XRS) the intensity of the solar X-ray flux (Goldsten et al. 2007; Schlemm et al. 2007). MAG will measure the vector magnetic field over six Mercury sidereal days (each 58.65 Earth days) under a range of solar distances and conditions, which should permit separation of internal and external fields sufficient to resolve Mercury's

quadrupole magnetic moment (Korth et al. 2004) and shorter-wavelength features near periapsis latitudes (Anderson et al. 2007). MLA will measure the topography of the northern hemisphere over four Mercury years (Cavanaugh et al. 2007). RS will extend topographic information to the southern hemisphere by occultation measurements of planet radius, and the planet's obliquity and the amplitude of the physical libration will be determined independently from the topography and gravity field (Srinivasan et al. 2007). The VIRS component of the MASCS instrument will produce global maps of surface reflectance from which mineralogy and its variation with geological unit can be inferred, and the UVVS component of the MASCS instrument will produce global maps of exospheric species abundances versus altitude and their temporal variations over four Mercury years and a range of solar activity (McClintock and Lankton 2007). EPPS will sample the plasma and energetic particle population in the solar wind, at major magnetospheric boundaries, and throughout the environment of Mercury at a range of solar distances and levels of solar activity (Andrews et al. 2007).

An additional important constraint on payload observing sequences is imposed by a rate of data downlink from the spacecraft to the DSN that varies strongly with time during the mission orbital phase (Fig. 16). The strategy to deal with such a variable data return is to store most data on the spacecraft solid-state recorder during periods when Mercury is far from Earth and to downlink combinations of stored data and newly acquired data during periods when Mercury is closest to Earth. A data prioritization scheme will assist in managing the downlink process. Under fairly conservative assumptions (downlinking to one 34-m

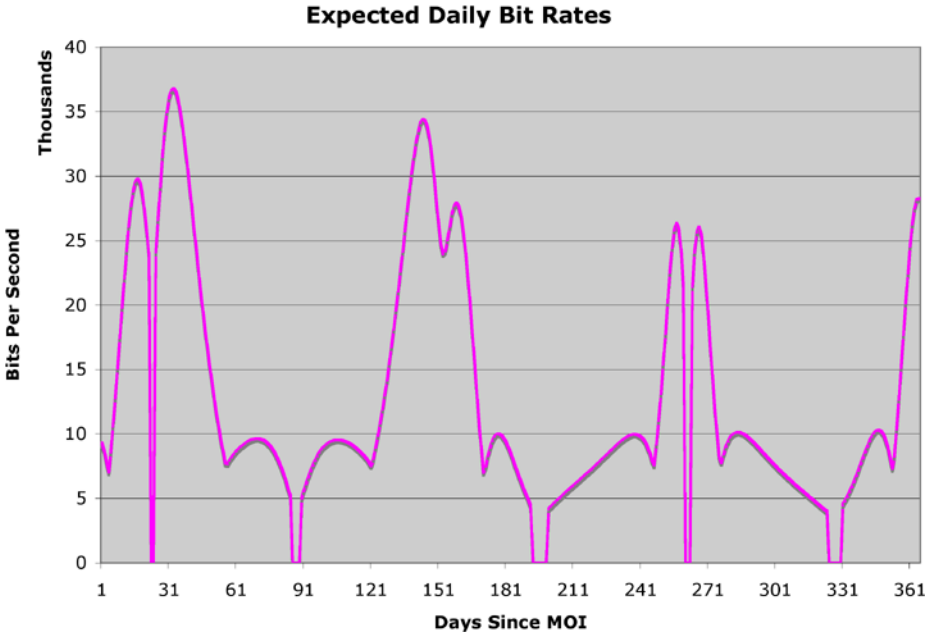

Fig. 16 Downlink data rates per day during the mission orbital phase. Peaks in the curve correspond to times near Mercury inferior conjunction; longer segments with zero data rate correspond to Mercury superior conjunction, and shorter segments correspond to times when Mercury passes between the Sun and Earth. This profile is based on the assumption that downlinked data will be received for 6.5 hours each day by one of the DSN 34-m antennas

DSN station for 6.5 hours per mission day) a total of more than 100 Gb of data will be returned during the mission orbital phase.

The orbital observation strategy is based on a combination of position along the orbit (northern polar zone, mid zone, and far zone as defined in Fig. 13) and a balance between available downlink and solid-state recorder resources. The exploratory nature of this mission requires built-in flexibility in the planning strategy in order to take maximum advantage of what is learned during the flybys and the early part of the orbital phase. Many of the instruments operate in conjunction with each other in observational campaigns that are defined by science objectives but are constrained by limits on data volumes. Margin and multiple opportunities for high-priority observations are therefore incorporated into the strategy where possible.

8 Data Products and Archiving

On the basis of its guiding science questions and measurement objectives, the MESSENGER project has defined a set of data products that will be produced primarily by the MESSENGER Science Team and archived with NASA's Planetary Data System (PDS). These data products and the schedule for delivering them to the PDS are defined in a formal MESSENGER Data Management and Science Analysis Plan (DMSAP) and are discussed in more detail in a companion article (Winters et al. 2007).

Planning and acquisition of science measurements are handled by MESSENGER's Science Planning Group (SPG). The SPG is responsible for ensuring that the data acquisition plan includes all observations needed to meet the mission's measurement objectives. These measurements are made available to the MESSENGER Science Team through the Science Operations Center (SOC). Data products that have been tagged for delivery to the PDS are generated by the MESSENGER Science Team and delivered to the SOC for submission to the PDS.

8.1 Data Validation

The SPG performs two types of validation processes to ensure that the instrument measurements meet all requirements for producing MESSENGER's data products. The validation process is divided into observation validation and observation quality verification. Observation validation ensures that those observations requested via the instrument command loads are actually executed and the expected measurements are returned to the SOC. Observation quality verification involves an examination of the returned data to ensure that they are of sufficient quality to meet the science objectives. The criteria on which the quality assessment is made is provided by MESSENGER's Science Steering Committee (Solomon et al. 2001).

Those observations that are not executed or returned to the SOC (for various reasons, such as loss of spacecraft function), or those observations which fail the quality assessment, are rescheduled in the data planning and commanding process. This information is conveyed to the Science Team via four discipline groups (Solomon et al. 2001) and the SPG. Both validation processes ensure that the data products produced by the MESSENGER team meet the mission's science objectives.

The data acquisition is monitored weekly by the SPG, and the progress toward meeting mission objectives is constantly assessed and reported to the Science Steering Committee. Coverage maps for each instrument's data set are generated daily to assess the mission's science objectives and to validate the data acquisition process.

8.2 Data Products

The data products produced by the MESSENGER mission are divided into two broad categories: raw data or Experimental Data Records (EDRs) and higher-level data products or Reduced Data Records (RDRs). The EDRs are formatted raw instrument data produced by the SOC directly from the spacecraft telemetry for use by the Science Team. The EDRs are used by the SOC and Science Team to produce the RDRs.

The RDRs have been divided into three groups: Calibrated Data Records (CDRs), Derived Data Products (DDPs), and Derived Analysis Products (DAPs). CDRs generally consist of EDR data that have been transformed into physical units. This transformation is done by either Science Team members or the SOC via algorithms provided by the Science Team. DDPs and DAPs are higher-level products produced by the Science Team and delivered to the SOC for submission to the PDS. These higher-level products may be constructed from observations made by more than one instrument. A list of the DDPs and DAPs that the MESSENGER project will be archiving to the PDS may be found in a companion paper (Winters et al. 2007).

8.3 Archiving Plan

The MESSENGER project is working closely with the PDS to facilitate the data archiving process, and toward that end a Data Archive Working Group (DAWG) was established early in the project (Solomon et al. 2001). Through this group the EDR and RDR data formats have been defined and described in instrument software interface specification (SIS) documents. These documents have been reviewed and approved by both the MESSENGER project and the PDS. These baseline efforts permit the archiving process to be streamlined, portions of the process to be automated, and the full delivery schedule for MESSENGER's data products (Winters et al. 2007) to be met.

During the MESSENGER mission there are several designated deliveries of data to the PDS (Winters et al. 2007), each associated with a mission milestone. The first four deliveries are, respectively, six months following the second Venus flyby (EDR data only) and six months following each of the Mercury flybys (EDRs and either calibration documentation or CDRs). Deliveries of orbital data (EDRs and CDRs) are scheduled at six-month intervals following orbit insertion. High-level RDR products (DDPs and DAPs) will be delivered to the PDS one year after the end of the mission, providing the Science Team adequate time to produce these products with the full MESSENGER data set.

9 Conclusions

The MESSENGER mission to Mercury will provide important new information on the formation and evolution of the inner planets. We will have obtained the first global views of Mercury's geology, exosphere, magnetic field, and magnetosphere. We will have ascertained the state and size of Mercury's core, fractionally the largest among the terrestrial planets. We will have learned about the nature of Mercury's polar deposits and what that nature implies for the sources of and storage mechanisms for near-surface volatiles. We will have carried out the first chemical remote sensing of Mercury's surface and from that information obtained new constraints on the planetary processes that led to Mercury's high ratio of metal to silicate. This new information will fuel a new understanding of planetary formation, the early history of the inner solar system, the origin of planetary magnetism, and modes of solar wind-magnetosphere interaction.

It is noteworthy that the MESSENGER mission is a product of NASA's Discovery Program, under which mission concepts are constrained at the outset by cost, schedule, and launch vehicle. Those constraints contributed to the extended duration of the mission cruise phase and limited the number of potential payload instruments. MESSENGER is nonetheless ambitious in its scientific scope for a Discovery mission, a tribute to the fact that scientific requirements guided the development of spacecraft (Leary et al. 2007) and mission design (McAdams et al. 2007) at every stage in the project, from initial concept through all design trades and testing. Those same science requirements now frame decisions made regularly in mission operations (Holdridge and Calloway 2007).

During and following the MESSENGER mission, the MESSENGER team will be working in close communication with the team now developing the BepiColombo mission, which involves the launch in 2013 of two spacecraft that will be inserted into Mercury orbit in 2019. Such communication is intended to ensure that the scientific return will be optimized from both missions (McNutt et al. 2004).

Acknowledgements The MESSENGER mission is supported by the NASA Discovery Program under contracts NASW-00002 to the Carnegie Institution of Washington and NAS5-97271 to The Johns Hopkins University Applied Physics Laboratory. We thank John Harmon, Andrew Potter, Mark Robinson, and James Slavin for permission to use figures; and we are grateful to Brian Anderson, John Cavanaugh, John Goldsten, Edward Hawkins, George Ho, James Leary, William McClintock, James McAdams, Charles Schlemm, Dipak Srinivasan, Richard Starr, Xiaoli Sun, Thomas Zurbuchen, and two anonymous reviewers for providing helpful comments on an earlier draft.

References

M.H. Acuña et al., Science **284**, 790–793 (1999)
O. Aharonson, M.T. Zuber, S.C. Solomon, Earth Planet. Sci. Lett. **218**, 261–268 (2004)
B.J. Anderson et al., Space Sci. Rev. (2007, this issue). doi:10.1007/s11214-007-9246-7
J.D. Anderson, G. Colombo, P.B. Esposito, E.L. Lau, G.B. Trager, Icarus **71**, 337–349 (1987)
G.B. Andrews et al., Space Sci. Rev. (2007, this issue). doi:10.1007/s11214-007-9272-5
A. Anselmi, G.E.N. Scoon, Planet. Space Sci. **49**, 1409–1420 (2001)
D.N. Baker, J.A. Simpson, J.H. Eraker, J. Geophys. Res. **91**, 8742–8748 (1986)
N.G. Barlow, R.A. Allen, F. Vilas, Icarus **141**, 194–204 (1999)
J. Baumgardner, M. Mendillo, J.K. Wilson, Astron. J. **119**, 2458–2464 (2000)
J.W. Belcher et al., Technical Memorandum 4255, NASA, Washington, DC, 1991, 132 pp
W. Benz, W.L. Slattery, A.G.W. Cameron, Icarus **74**, 516–528 (1988)
T.A. Bida, R.M. Killen, T.H. Morgan, Nature **404**, 159–161 (2000)
B.G. Bills, Lunar Planet. Sci. **33** (2002), abstract 1599
D.T. Blewett, P.G. Lucey, B.R. Hawke, G.G. Ling, M.S. Robinson, Icarus **129**, 217–231 (1997)
D.T. Blewett, B.R. Hawke, P.G. Lucey, Meteorit. Planet. Sci. **37**, 1245–1254 (2002)
D.T. Blewett, B.R. Hawke, P.G. Lucey, M.S. Robinson, J. Geophys. Res. **112**, E02005 (2007). doi:10.1029/2006JE002713
W.V. Boynton et al., Space Sci. Rev. (2007). doi:10.1007/s11214-007-9258-3
A.L. Broadfoot, S. Kumar, M.J.S. Belton, M.B. McElroy, Science **185**, 166–169 (1974)
A.L. Broadfoot, D.E. Shemansky, S. Kumar, Geophys. Res. Lett. **3**, 577–580 (1976)
T.H. Burbine, T.J. McCoy, L.R. Nittler, G.K. Benedix, E.A. Cloutis, T.L. Dickinson, Meteorit. Planet. Sci. **37**, 1233–1244 (2002)
A.G.W. Cameron, Icarus **64**, 285–294 (1985)
J.F. Cavanaugh et al., Space Sci. Rev. (2007, this issue). doi:10.1007/s11214-007-9273-4
S.C. Chase, E.D. Miner, D. Morrison, G. Münch, G. Neugebauer, M. Schroeder, Science **185**, 142–145 (1974)
A.F. Cheng, R.E. Johnson, S.M. Krimigis, L.J. Lanzerotti, Icarus **71**, 430–440 (1987)
U.R. Christensen, Nature **444**, 1056–1058 (2006)
S.P. Christon, Icarus **71**, 448–471 (1987)
P.E. Clark, S. Curtis, B. Giles, G. Marr, C. Eyerman, D. Winterhalter, Lunar Planet. Sci. **30** (1999), abstract 1036

COMPLEX, *Strategy for Exploration of the Inner Planets: 1977–1987* (Committee on Lunar and Planetary Exploration, National Academy of Sciences, Washington, 1978), 97 pp
COMPLEX, *1990 Update to Strategy for Exploration of the Inner Planets* (Committee on Lunar and Planetary Exploration, National Academy Press, Washington, 1990), 47 pp
J.E.P. Connerney, N.F. Ness, in *Mercury*, ed. by F. Vilas, C.R. Chapman, M.S. Matthews (University of Arizona Press, Tucson, 1988), pp. 494–513
A.C. Cook, M.S. Robinson, J. Geophys. Res. **105**, 9429–9443 (2000)
R.F. Dantowitz, S.W. Teare, M.J. Kozubal, Astron. J. **119**, 2455–2457 (2000)
D.L. Domingue et al., Space Sci. Rev. (2007, this issue). doi:10.1007/s11214-007-9260-9
J.H. Eraker, J.A. Simpson, J. Geophys. Res. **91**, 9973–9993 (1986)
B. Fegley Jr., A.G.W. Cameron, Earth Planet. Sci. Lett. **82**, 207–222 (1987)
W.C. Feldman, B.L. Barraclough, C.J. Hansen, A.L. Sprague, J. Geophys. Res. **102**, 25565–25574 (1997)
G. Giampieri, A. Balogh, Planet. Space Sci. **50**, 757–762 (2002)
R.E. Gold et al., Planet. Space Sci **49**, 1467–1479 (2001)
J.O. Goldsten et al., Space Sci. Rev. (2007, this issue). doi:10.1007/s11214-007-9262-7
R. Grard, M. Novara, G. Scoon, ESA Bull. **103**, 11–19 (2000)
H. Harder, G. Schubert, Icarus **151**, 118–122 (2001)
J.K. Harmon, Adv. Space Res. **19**, 1487–1496 (1997)
J.K. Harmon, Lunar Planet. Sci. **33** (2002), abstract 1858
J.K. Harmon, M.A. Slade, Science **258**, 640–642 (1992)
J.K. Harmon, P.J. Perillat, M.A. Slade, Icarus **149**, 1–15 (2001)
J.K. Harmon, M.A. Slade, B.J. Butler, J.W. Head, III, M.S. Rice, D.B. Campbell, Icarus **187**, 374–405 (2007)
S.A. Hauck, II, A.J. Dombard, R.J. Phillips, S.C. Solomon, Earth Planet. Sci. Lett. **222**, 713–728 (2004)
S.E. Hawkins, III et al., Space Sci. Rev. (2007, this issue). doi:10.1007/s11214-007-9266-3
H. Hayakawa, Y. Kasaba, H. Yamakawa, H. Ogawa, T. Mukai, Adv. Space Res. **33**, 2142–2146 (2004)
J.W. Head et al., Space Sci. Rev. (2007, this issue). doi:10.1007/s11214-007-9263-6
M.H. Heimpel, J.M. Aurnou, F.M. Al-Shamali, N. Gomez Perez, Earth Planet. Sci. Lett. **236**, 542–557 (2005)
M.E. Holdridge, A.B. Calloway, Space Sci. Rev. (2007, this issue). doi:10.1007/s11214-007-9261-8
I.V. Holin, Lunar Planet. Sci. **33** (2002), abstract 1387
L.L. Hood, G. Schubert, J. Geophys. Res. **84**, 2641–2647 (1979)
D.M. Hunten, A.L. Sprague, Meteorit. Planet. Sci. **37**, 1191–1195 (2002)
D.M. Hunten, T.H. Morgan, D.E. Shemansky, in *Mercury*, ed. by F. Vilas, C.R. Chapman, M.S. Matthews (University of Arizona Press, Tucson, 1988), pp. 562–612
P. Janhunen, E. Kallio, Ann. Geophys. **22**, 1829–1830 (2004)
R. Jeanloz, D.L. Mitchell, A.L. Sprague, I. de Pater, Science **268**, 1455–1457 (1995)
R.M. Killen, J. Benkhoff, T.H. Morgan, Icarus **125**, 195–211 (1997)
R.M. Killen, A. Potter, A. Fitzsimmons, T.H. Morgan, Planet. Space Sci. **47**, 1449–1458 (1999)
R.M. Killen et al., J. Geophys. Res. **106**, 20509–20525 (2001)
G. Kletetschka, P. Wasilewski, P.T. Taylor, Meteorit. Planet. Sci. **35**, 895–899 (2000)
S.J. Kortenkamp, E. Kokubo, S.J. Weidenschilling, in *Origin of the Earth and Moon*, ed. by R.M. Canup, K. Righter (University of Arizona Press, Tucson, 2000), pp. 85–100
H. Korth et al., Planet. Space Sci. **52**, 733–746 (2004)
L. Ksanfomality, A.L. Sprague, Icarus **188**, 271–287 (2007)
L. Ksanfomality, G. Papamastorakis, N. Thomas, Planet. Space Sci. **53**, 849–859 (2005)
J.C. Leary et al., Space Sci. Rev. (2007, this issue). doi:10.1007/s11214-007-9269-0
F. Leblanc, R.E. Johnson, Icarus **164**, 261–281 (2003)
V. Lesur, A. Jackson, Geophys. J. Int. **140**, 453–459 (2000)
J.S. Lewis, in *Mercury*, ed. by F. Vilas, C.R. Chapman, M.S. Matthews (University of Arizona Press, Tucson, 1988), pp. 651–669
J.L. Margot, S.J. Peale, R.F. Jurgens, M.A. Slade, I.V. Holin, Science **316**, 710–714 (2007)
J.V. McAdams, R.W. Farquhar, A.H. Taylor, B.G. Williams, Space Sci. Rev. (2007, this issue). doi:10.1007/s11214-007-9162-x
W.E. McClintock, M.R. Lankton, Space Sci. Rev. (2007, this issue). doi:10.1007/s11214-007-9264-5
R.L. McNutt Jr., S.C. Solomon, R. Grard, M. Novara, T. Mukai, Adv. Space Res. **33**, 2126–2132 (2004)
R.L. McNutt Jr., S.C. Solomon, R.E. Gold, J.C. Leary, the MESSENGER Team, Adv. Space Res. **38**, 564–571 (2006)
M. Mendillo, J. Warell, S.S. Limaye, J. Baumgardner, A. Sprague, J.K. Wilson, Planet. Space Sci. **49**, 1501–1505 (2001)
S.M. Milkovich, J.W. Head, L. Wilson, Meteorit. Planet. Sci. **37**, 1209–1222 (2002)
J.I. Moses, K. Rawlins, K. Zahnle, L. Dones, Icarus **137**, 197–221 (1999)
B.C. Murray, J. Geophys. Res. **80**, 2342–2344 (1975)

V.R. Murthy, W. van Westrenen, Y. Fei, Nature **423**, 163–165 (2003)
R.M. Nelson, L.J. Horn, J.R. Weiss, W.D. Smythe, Lunar Planet. Sci. **25**, 985–986 (1994)
N.F. Ness, K.W. Behannon, R.P. Lepping, Y.C. Whang, K.H. Schatten, Science **185**, 151–160 (1974)
N.F. Ness, K.W. Behannon, R.P. Lepping, Y.C. Whang, J. Geophys. Res. **80**, 2708–2716 (1975)
N.F. Ness, K.W. Behannon, R.P. Lepping, Y.C. Whang, Icarus **28**, 479–488 (1976)
G. Neukum et al., Mercury polar orbiter, A proposal to the European Space Agency in response to a call for new mission proposals issued on 10 July 1985, Deutsche Forschungs- und Versuchsanstalt für Luft- und Raumfahrt, Wessling, Germany, 1985, 33 pp
G. Neukum, J. Oberst, H. Hoffmann, R. Wagner, B.A. Ivanov, Planet. Space Sci. **49**, 1507–1521 (2001)
F. Nimmo, Geophys. Res. Lett. **29**, 1063 (2002). doi:10.1029/2001GL013883
F. Nimmo, T.R. Watters, Geophys. Res. Lett. **31**, L02701 (2004). doi:10.1029/2003GL018847
K.W. Ogilvie et al., Science **185**, 145–151 (1974). doi:10.1029/2003GL018847
D.A. Paige, S.E. Wood, A.R. Vasavada, Science **258**, 643–646 (1992)
S.J. Peale, in *Mercury*, ed. by F. Vilas, C.R. Chapman, M.S. Matthews (University of Arizona Press, Tucson, 1988), pp. 461–493
S.J. Peale, R.J. Phillips, S.C. Solomon, D.E. Smith, M.T. Zuber, Meteorit. Planet. Sci. **37**, 1269–1283 (2002)
A.E. Potter, T.H. Morgan, Science **229**, 651–653 (1985)
A.E. Potter, T.H. Morgan, Icarus **67**, 336–340 (1986)
A.E. Potter, R.M. Killen, T.H. Morgan, Planet. Space Sci. **47**, 1441–1448 (1999)
A.E. Potter, R.M. Killen, T.H. Morgan, Meteorit. Planet. Sci. **37**, 1165–1172 (2002a)
A.E. Potter, C.M. Anderson, R.M. Killen, T.H. Morgan, J. Geophys. Res. **107**, 5040 (2002b). doi:10.1029/2000JE001493
M.S. Robinson, P.G. Lucey, Science **275**, 197–198 (1997)
M.S. Robinson, G.J. Taylor, Meteorit. Planet. Sci. **36**, 841–847 (2001)
M.S. Robinson, M.E. Davies, T.R. Colvin, K. Edwards, J. Geophys. Res. **104**, 30847–30852 (1999)
S.K. Runcorn, Nature **253**, 701–703 (1975)
A.G. Santo et al., Planet. Space Sci. **49**, 1481–1500 (2001)
C.E. Schlemm II, et al., Space Sci. Rev. (2007, this issue). doi:10.1007/s11214-007-9248-5
G. Schubert, M.N. Ross, D.J. Stevenson, T. Spohn, in *Mercury*, ed. by F. Vilas, C.R. Chapman, M.S. Matthews (University of Arizona Press, Tucson, 1988), pp. 429–460
R. Schulz, J. Benkhoff, Adv. Space Res. **38**, 572–577 (2006)
R.W. Siegfried, II, S.C. Solomon, Icarus **23**, 192–205 (1974)
J.A. Simpson, J.H. Eraker, J.E. Lamport, P.H. Walpole, Science **185**, 160–166 (1974)
G. Siscoe, L. Christopher, Geophys. Res. Lett. **2**, 158–160 (1975)
M.A. Slade, B.J. Butler, D.O. Muhleman, Science **258**, 635–640 (1992)
M.A. Slade, R.F. Jurgens, J.-L. Margot, E.M. Standish, in *Mercury: Space Environment, Surface, and Interior* (Lunar and Planetary Institute, Houston, 2001), pp. 88–89
J.A. Slavin, Adv. Space Res. **33**, 1859–1874 (2004)
J.A. Slavin et al., Space Sci. Rev. (2007, this issue). doi:10.1007/s11214-007-9154-x
D.E. Smith, M.T. Zuber, S.J. Peale, R.J. Phillips, S.C. Solomon, in *Mercury: Space Environment, Surface, and Interior* (Lunar and Planetary Institute, Houston, 2001), pp. 90–91
D.E. Smith et al., Science **311**, 53 (2006)
S.C. Solomon et al., Planet. Space Sci. **49**, 1445–1465 (2001)
A.L. Sprague, D.M. Hunten, K. Lodders, Icarus **118**, 211–215 (1995)
A.L. Sprague et al., Icarus **129**, 506–527 (1997)
A.L. Sprague, W.J. Schmitt, R.E. Hill, Icarus **136**, 60–68 (1998)
A.L. Sprague, J.P. Emery, K.L. Donaldson, R.W. Russell, D.K. Lynch, A.L. Mazuk, Meteorit. Planet. Sci. **37**, 1255–1268 (2002)
P.D. Spudis, J.E. Guest, in *Mercury*, ed. by F. Vilas, C.R. Chapman, M.S. Matthews (University of Arizona Press, Tucson, 1988), pp. 118–164
P.D. Spudis, J.B. Plescia, A.D. Stewart, Lunar Planet. Sci. **25**, 1323–1324 (1994)
D.K. Srinivasan, M.E. Perry, K.B. Fielhauer, D.E. Smith, M.T. Zuber, Space Sci. Rev. (2007, this issue). doi:10.1007/s11214-007-9270-7
L.J. Srnka, Phys. Earth Planet. Inter. **11**, 184–190 (1976)
S. Stanley, J. Bloxham, W.E. Hutchison, M.T. Zuber, Earth Planet. Sci. Lett. **234**, 27–38 (2005)
L.V. Starukhina, J. Geophys. Res. **106**, 14701–14710 (2001)
A. Stephenson, Earth Planet. Sci. Lett. **28**, 454–458 (1976)
D.J. Stevenson, Earth Planet. Sci. Lett. **82**, 114–120 (1987)
D.J. Stevenson, Earth Planet. Sci. Lett. **208**, 1–11 (2003)
R.G. Strom, N.J. Trask, J.E. Guest, J. Geophys. Res. **80**, 2478–2507 (1975)

H. Svedhem, D. Titov, D. McCoy, J. Rodriguez-Canabal, J. Fabrega, Eos, Trans. Am. Geophys. Union **86** (Fall Meeting suppl.) (2005), abstract P23E-01
A.R. Vasavada, D.A. Paige, S.E. Wood, Icarus **141**, 179–193 (1999)
F. Vilas, Icarus **64**, 133–138 (1985)
J. Warell, S.S. Limaye, Planet. Space Sci. **49**, 1531–1552 (2001)
J. Warell, P.-G. Valegård, Astron. Astrophys. **460**, 625–633 (2006)
J. Warell, A.L. Sprague, J.P. Emery, R.W.H. Kozlowski, A. Long, Icarus **35**, 99–111 (2006)
T.R. Watters, M.S. Robinson, A.C. Cook, Geology **26**, 991–994 (1998)
T.R. Watters, R.A. Schultz, M.S. Robinson, A.C. Cook, Geophys. Res. Lett. **29**, 1542 (2002). doi:10.1029/2001GL014308
S.J. Weidenschilling, Icarus **35**, 99–111 (1978)
S.J. Weidenschilling, Lunar Planet. Sci. **29** (1998), abstract 1278
S.J. Weidenschilling, J.N. Cuzzi, in *Protostars and Planets III*, ed. by E.H. Levy, J.I. Lunine (University of Arizona Press, Tucson, 1993), pp. 1031–1060
G.W. Wetherill, in *Mercury*, ed. by F. Vilas, C.R. Chapman, M.S. Matthews (University of Arizona Press, Tucson, 1988), pp. 670–691
G.W. Wetherill, Geochim. Cosmochim. Acta **58**, 4513–4520 (1994)
H.L. Winters et al., Space Sci. Rev. (2007, this issue). doi:10.1007/s11214-007-9257-4
X. Wu, P.L. Bender, S.J. Peale, G.W. Rosborough, M.A. Vincent, Planet. Space Sci. **45**, 15–19 (1997)
C.-W. Yen, Ballistic Mercury orbiter mission via Venus and Mercury gravity assists, AAS/AIAA Astrodynamics Specialist Conference, AIAA 83-346, San Diego, CA (1985)
C.-W. Yen, J. Astronaut. Sci. **37**, 417–432 (1989)
M.T. Zuber et al., Space Sci. Rev. (2007, this issue). doi:10.1007/s11214-007-9265-4